Ecological Modelling 510 (2025) 111318

Contents lists available at ScienceDirect

Ecological Modelling

journal homepage: www.elsevier.com/locate/ecolmodel

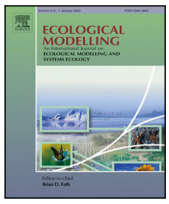

# A spatiotemporal SEIR model for predicting wheat stripe and leaf rusts epidemics

Mustapha El Jarroudi [a], Hasan Karjoun [b,*], Riane Hajjami [c], Louis Kouadio [d,e], Moussa El Jarroudi [f]

[a] Department of Mathematics, FST Tanger, Abdelmalek Essaadi University, B.P.416, Tangier, Morocco
[b] 2IACS Laboratory, ENSET Mohammedia, Hassan II University of Casablanca, Morocco
[c] LSIA Laboratory, Moroccan School of Engineering Sciences (EMSI), Tangier, Morocco
[d] Africa Rice Center (AfricaRice), Bouake, Ivory Coast
[e] Centre for Applied Climate Sciences, University of Southern Queensland, Toowoomba, Queensland, Australia
[f] Water, Environment and Development Unit, UR SPHERES, Department of Environmental Sciences and Management, University of Liège, Arlon, Belgium

ARTICLE INFO

*Keywords:*
Spatiotemporal SEIR model
Spores dispersal
Wind-borne pathogens
Numerical simulations
UAV- based imagery
Disease severity

ABSTRACT

Understanding the dynamics and severity of foliar fungal diseases in space and time is crucial to ensure effective epidemic control. Here, we presented a Susceptible-Exposed-Infected-Removed (SEIR) modeling approach integrating a nonlocal dispersion model of wind-borne pathogens and meteorological factors to describe the dynamics of wheat stripe rust (WSR) and wheat leaf rust (WLR). Variations of wheat plant populations from one compartment to another were modeled with weather dependent probabilities based on defined assumptions for the host population and wind velocity. The well-posedness of the formulated model was established and the final size of the epidemic was theoretically determined. Data for the 2018/2019 wheat cropping season from four representative wheat-growing regions in Luxembourg were used to fit the SEIR model for each disease and evaluate its capability to simulate disease progress and severity. Numerical simulations were carried out to visually assess the spatiotemporal patterns of the $S$, $E$, $I$, and $R$ compartments over a two-dimensions computational domain during the period of May to July 2019, which corresponds to the critical period of WSR and WLR development at the study sites. The SEIR model was fitted using unmanned aerial vehicle (UAV) imagery data for both WSR and WLR, and overall, the results showed a good fit between the simulated disease severity and the UAV-derived estimates.

## 1. Introduction

Globally, crop yield losses due to plant diseases are estimated to cost approximately US$220 billion annually (FAO, 2019). Effective disease management requires a multifaceted approach that combines prevention, monitoring, and control strategies. A critical component of this effort is understanding the key drivers of disease outbreaks (e.g., environmental factors and cropping systems) and their spatial and temporal patterns of incidence and severity. One promising approach to support this understanding is the use of mathematical models, which integrate diverse biological, environmental, and epidemiological factors (Gilligan and van den Bosch, 2008; Cunniffe et al., 2015; Rimbaud et al., 2018; Diekmann et al., 2021).

A variety of mathematical models, including compartmental models, have been developed to explore the spatial and temporal dynamic interactions between host plants, pathogens, and the environment (see for a comprehensive review Cooke et al., 2006; Madden et al., 2007; Gilligan, 2008). Compartmental models such as Susceptible-Infected-Removed (SIR) models and Susceptible-Exposed-Infected-Removed (or Recovered) (SEIR), are particularly valued for their extensibility and flexibility (Gilligan et al., 1997; Diekmann and Heesterbeek, 2000; Segarra et al., 2001; Soubeyrand et al., 2008; Cunniffe et al., 2012). The compartmental modeling approach simplifies complex biological interactions, making it easier to analyze disease spread within and between plant populations. By incorporating factors like infection rates, recovery rates, and transmission probabilities, these models can simulate the risk of disease outbreaks under varying conditions including weather, plant density, and prior disease incidence, which can support the development of timely and effective control strategies (Gibson

* Corresponding author.
*E-mail address:* hasan.karjoun@etu.univh2c.ma (H. Karjoun).

https://doi.org/10.1016/j.ecolmodel.2025.111318
Received 14 March 2025; Received in revised form 8 August 2025; Accepted 13 August 2025
Available online 26 August 2025

et al., 2004; Cunniffe et al., 2015; Rimbaud et al., 2018). The use of SIR model and its variants to investigate the spatiotemporal spread of fungal pathogens responsible for foliar diseases is well established. For instance, SIR models have been applied to study rusts in cereal crops (e.g., Soubeyrand et al., 2008; Rimbaud et al., 2018; El Jarroudi et al., 2020), fusarium head blight in wheat (Xiao et al., 2022), stem canker disease and late blight in potato (e.g., Gilligan et al., 1997; Narouei-Khandan et al., 2020), powdery mildew in grapevine (Burie et al., 2008), and various rice diseases including brown spot and blast, bacterial blight, sheath blight, and rice tungro disease (e.g., Savary et al., 2012; Kirtphaiboon et al., 2021; Tabonglek et al., 2022). Despite their demonstrated utility, the accurate parameterization and broader applicability of compartmental models remain constrained by limited datasets on pathogen biology, host-pathogen interactions, and long-term dynamics (Cunniffe et al., 2015; Rimbaud et al., 2018). These gaps pose significant challenges to model scalability and transferability across diverse environmental conditions.

For various economically important plant diseases caused by pathogenic fungi, the main route of spore dispersal is wind or rain-splash (Zadoks, 1971; Eversmeyer et al., 1988; Madden, 1997; Hau and de Vallavieille-Pope, 2006). The dispersal of biological organisms has been extensively documented (e.g., Othmer et al., 1988; Frantzen and van den Bosch, 2000; Sackett and Mundt, 2005; Soubeyrand et al., 2008; Mikaberidze et al., 2016; Rimbaud et al., 2018; El Jarroudi et al., 2020). For example, Soubeyrand et al. (2008) employed a combination of horizontal and vertical dispersal functions to model the three-dimensional dispersal of *Puccinia striiformis* spores (the causing pathogen of WSR) in a wheat field in France. Modeling approaches integrating nonlocal spore dispersal models and meteorological factors were also developed for wheat rusts in Luxembourg (El Jarroudi et al., 2020) and rice blast disease in Thailand (Tabonglek et al., 2022). In the former study, the dispersal model integrates variations in wind velocity components and a threshold in the convolution kernel defining the non-local diffusion term (El Jarroudi et al., 2020). A similar modeling approach for pathogen spore dispersal was adopted in Tabonglek et al. (2022), with the consideration of rain splash factor being the main difference between the two modeling approaches. However, demonstrating the ability of SEIR models that integrate nonlocal spore dispersal model, weather-dependent latency periods, and wind velocity variability to realistically simulate the dynamics of WSR (caused by *Puccinia striiformis*) and WLR (caused by *Puccinia triticina*) epidemics under field conditions, characterized by fluctuations in temperature, relative humidity and wind velocity, remains an open research challenge.

The proposed model builds upon the framework developed by Rimbaud et al. (2018); a genetic-dynamic model that integrates both demographic changes in pathogen populations and genetic evolution to simulate the spatiotemporal spread of pathogens within cropping landscapes. The model's potential to assess the durability and effectiveness of combinations of qualitative and quantitative resistance sources for controlling rusts in cereal crops was evaluated using simulated landscape structures (Rimbaud et al., 2018). While the model offers several valuable features (e.g., flexible parameterization, possibility to vary the epidemiology and the evolutionary potential of the pathogen, ability to parameterize the model to biotrophic and necrotrophic fungal pathogens), it still faces challenges in calibrating certain parameters, particularly those related to sporulation rate and dispersal kernels. These difficulties arise mainly due to limited availability of relevant field data and the poor representativeness of controlled-environment data (Rimbaud et al., 2018). One way to address these challenges is to build models based on parameter estimates derived from field observations. Several methods exist for parameter estimation, including recent approaches that leverage machine learning algorithms to infer parameters from data and use validation to ensure adequate estimates.

In this study, a SEIR epidemiological modeling approach integrating a nonlocal dispersion model of windborne pathogens and meteorological factors was proposed to describe the spatiotemporal dynamics of WSR and WLR. The modeling approach followed those of Segarra et al. (2001) and Cunniffe et al. (2015). It is an expansion of the mathematical model for spore dispersal described in El Jarroudi et al. (2020) through the integration of temperature-dependent latency periods and an improved modeling of the different compartments. With the overarching purpose of improving WSR and WLR management, such models can provide insightful information into disease severity and serve as a basis for decision support tools.

## 2. Theoretical modeling approach

### 2.1. Background

The vertical dimension of the crop, which is much smaller than the horizontal one, is neglected. We assume that the time and space variables are represented by continuous parameters, the crop fills in a bounded domain $\Omega \subset \mathbb{R}^2$, and the domain $\Omega$ is symmetric with respect to the origin. We denote by:

- $S(\boldsymbol{x},t)$ the density of susceptible hosts at position $\boldsymbol{x}$ and time $t$.
- $E(\boldsymbol{x},t)$ the density of exposed plants at position $\boldsymbol{x}$ and time $t$ (that are infected individuals in the latency period).
- $I(\boldsymbol{x},t)$ the density of infectious individuals at position $\boldsymbol{x}$ and time $t$.
- $R(\boldsymbol{x},t)$ the density of removed individuals at position $\boldsymbol{x}$ and time $t$.

Let $u(\boldsymbol{x},t)$ be the density of spores produced by an infectious individual at time $t$ and position $\boldsymbol{x}$. The spore dispersal is modeled using a nonlocal diffusion equation which takes into account variations in wind velocity components

$$\frac{\partial u}{\partial t}(\boldsymbol{x},t) = \int_{\Omega} J(\boldsymbol{x}-\boldsymbol{y})\,(u(\boldsymbol{y},t)-u(\boldsymbol{x},t))\,d\boldsymbol{y} + f(u(\boldsymbol{x},t)), \tag{1}$$

in $\Omega\times(0,\infty)$, where $\boldsymbol{x}=(x_1,x_2)$ and $\boldsymbol{y}=(y_1,y_2)$ are the space points in $\Omega\subset\mathbb{R}^2$ and $J(\boldsymbol{x}-\boldsymbol{y})\,d\boldsymbol{y}$ is the probability that an individual pathogen migrates from a position $\boldsymbol{y}$ to a position $\boldsymbol{x}$. The term

$$\int_{\Omega} J(\boldsymbol{x}-\boldsymbol{y})\,(u(\boldsymbol{y},t)-u(\boldsymbol{x},t))\,d\boldsymbol{y}$$

takes into account the pathogens arriving at position $\boldsymbol{x}$ from all other places or leaving this location to travel to all other sites; $f(u(\boldsymbol{x},t))$ corresponds to the density of new pathogens at site $\boldsymbol{x}$ and time $t$. Eq. (1) involves a nonlocal diffusion term $(J*u)(\boldsymbol{x},t)=\int_{\Omega} J(\boldsymbol{x}-\boldsymbol{y})\,u(\boldsymbol{y},t)\,d\boldsymbol{y}$ which depends on all values of $u$ in the neighborhood of $\boldsymbol{x}$. This diffusion operator characterizes the movements and interactions of species between non-adjacent spatial locations. It has been used to model diffusion processes in biological and physical problems (e.g., Bates et al., 1997; Pan et al., 2009; Gourley and Wu, 2006; Andreu-Vaillo et al., 2010).

### 2.2. Model formulation

WLR and WSR are marked by the capacity of their causal agents *Puccinia triticina* and *P. striiformis Westend*, respectively to produce urediniospores that can be wind-disseminated within crops, and infect susceptible plant hosts (Hau and de Vallavieille-Pope, 2006). To describe this dual nature of disease dynamics, local infection at the host level and nonlocal transmission via airborne spore dispersal, we propose the following reaction–diffusion model with a nonlocal dispersal term:

$$\begin{cases} \dfrac{\partial S}{\partial t}(\boldsymbol{x},t) &= -\alpha(t)(uS)(\boldsymbol{x},t) & \text{in } \Omega\times(0,+\infty), \\ \dfrac{\partial E}{\partial t}(\boldsymbol{x},t) &= \alpha(t)(uS)(\boldsymbol{x},t)-\eta(t)E(\boldsymbol{x},t) & \text{in } \Omega\times(0,+\infty), \\ \dfrac{\partial I}{\partial t}(\boldsymbol{x},t) &= \eta(t)E(\boldsymbol{x},t)-\beta I(\boldsymbol{x},t) & \text{in } \Omega\times(0,+\infty), \\ \dfrac{\partial R}{\partial t}(\boldsymbol{x},t) &= \beta I(\boldsymbol{x},t) & \text{in } \Omega\times(0,+\infty), \\ \dfrac{\partial u}{\partial t}(\boldsymbol{x},t) &= \displaystyle\int_{\Omega} J(\boldsymbol{x}-\boldsymbol{y})(u(\boldsymbol{y},t)-u(\boldsymbol{x},t))\,d\boldsymbol{y} \\ &\quad + f(u(\boldsymbol{x},t)) & \text{in } \Omega\times(0,+\infty), \end{cases} \tag{2}$$

with the following initial condition

$$\begin{cases} S(\boldsymbol{x},0) &= S_0(\boldsymbol{x})>0,\ E(\boldsymbol{x},0)=E_0\geq 0 & \text{in } \Omega, \\ I(\boldsymbol{x},0) &= I_0(\boldsymbol{x})\geq 0,\ R(\boldsymbol{x},0)=R_0(\boldsymbol{x})\geq 0 & \text{in } \Omega, \\ u(\boldsymbol{x},0) &= u_0(\boldsymbol{x}) & \text{in } \Omega, \end{cases} \tag{3}$$

where the term $(uS)(\boldsymbol{x},t)$ designates the contact between pathogens and susceptible individual plants at position $\boldsymbol{x}$ and time $t$, the term $\alpha(t)(uS)(\boldsymbol{x},t)$ represents, according to the law of mass-action (see for instance (Diekmann and Heesterbeek, 2000, Chapter 10)), the rate at which susceptible individuals become infected.

The parameter $\alpha$ is the probability (homogeneous in space) that a pathogen inoculates a susceptible individual, which depends on varying temperature and wetness conditions, $\eta(t) := 1/LP(t)$ is the probability that an exposed individual reaches the end of its latency period $LP$ and becomes infectious, and $\beta$ is the homogeneous probability per unit time that an individual reaches the end of the infectious period.

The parameter $\alpha$ is described as follows (de Vallavieille-Pope et al., 1995):

$$\alpha(t) = \mu \Phi_{\max} \Phi_T(t) \Phi_W(t), \tag{4}$$

where $\mu$ is the homogeneous probability per unit time for spore deposition on the crop, $\Phi_{\max}$ is the maximum infection efficiency, and

$$\Phi_T(t) = \sigma \left(\frac{T(t)-T_{\min}}{T_{\max}-T_{\min}}\right)^n \left(\frac{T_{\max}-T(t)}{T_{max}-T_{\min}}\right)^m,$$

$$\Phi_W(t) = 1-\exp\left(-d\left(RH(t)-W_{\min}\right)\right),$$

where $T(t)$ is the temperature at time $t$, $T_{\min}$ and $T_{\max}$ refer to the minimum and maximum air temperatures, respectively; $RH(t)$ is the time-varying relative air humidity; $W_{\min}$ is the minimum wetness period for infection; and $d$, $n$, $m$ and $\sigma$ are the shape parameters with

$$\sigma = \frac{(n+m)^{n+m}}{n^n m^m}.$$

Note that the model includes a temperature-dependent latency period, which is an improvement of the model developed in El Jarroudi et al. (2020). The equations of the latency periods for each disease are provided in Section 3.7.

The source term $f(u)$, which corresponds to the production of pathogens by infectious hosts at position $\boldsymbol{x}$ and time $t$, is taken as

$$f(u(\boldsymbol{x},t)) = \kappa \int_0^t \alpha(t-s)(uS)(\boldsymbol{x},t-s)\,\varpi(s)\,ds, \tag{5}$$

where $\kappa$ is the average number of pathogen particles produced per host infected that reach the end of sporulation stage; $\varpi$ is the sporulation curve described by the delayed-gamma distribution (Madden et al., 2007):

$$\varpi(s) = \begin{cases} 0 & \text{if } s<\tau, \\ \dfrac{a^b (s-\tau)^{b-1} e^{-a(s-\tau)}}{\Gamma(b)} & \text{if } s\geq\tau, \end{cases} \tag{6}$$

where $\tau$ is the mean value of the latency period $LP$, and $a$, $b$ are the shape parameters of the sporulation curve. According to Madden et al. (2007) and Cunniffe et al. (2012), the quantity

$$\kappa\alpha(t-s)(uS)(\boldsymbol{x},t-s)\,\varpi(s) = -\kappa\frac{dS(\boldsymbol{x},t-s)}{dt}\varpi(s),$$

is the number of infections produced by $s$ units of time and, therefore, that have infectivity $\varpi(s)$ at time $t$, and the integral in Eq. (5) represents the cumulative production of spores by all infected hosts according to time since infection.

**Remark 1.** We supposed that, at each site $\boldsymbol{x}$, the total plant population denoted by $N(\boldsymbol{x})$ is independent of time. That is

$$S(\boldsymbol{x},t)+E(\boldsymbol{x},t)+I(\boldsymbol{x},t)+R(\boldsymbol{x},t)=N(\boldsymbol{x}).$$

Then introducing the new scaling

$$\begin{array}{lllllll} S(\boldsymbol{x},t) & := & S(\boldsymbol{x},t)/N(\boldsymbol{x}), & E(x,t) & := & E(\boldsymbol{x},t)/N(\boldsymbol{x}), \\ I(\boldsymbol{x},t) & := & I(\boldsymbol{x},t)/N(\boldsymbol{x}), & R(\boldsymbol{x},t) & := & R(\boldsymbol{x},t)/N(\boldsymbol{x}), \end{array} \tag{7}$$

we infer that the total plant density, at any site and any time, verifies

$$S(\boldsymbol{x},t)+E(\boldsymbol{x},t)+I(\boldsymbol{x},t)+R(\boldsymbol{x},t)=1. \tag{8}$$

Pathogens may not enter or leave the domain $\Omega$. Thus, spore dispersal only takes place in $\Omega$. This is the analogous of what is called homogeneous Neumann boundary condition $\dfrac{\partial u}{\partial n}=0$ on $\partial\Omega$ for partial differential equations. It is a simplified case of the general Neumann boundary condition in nonlocal diffusion problems:

$$\begin{aligned} \frac{\partial u}{\partial t}(\boldsymbol{x},t) &= \int_{\Omega} J(\boldsymbol{x}-\boldsymbol{y})(u(\boldsymbol{y},t)-u(\boldsymbol{x},t))\,d\boldsymbol{y}+f(u(\boldsymbol{x},t)) \\ &\quad + \int_{\mathbb{R}^2\setminus\Omega} J(\boldsymbol{x}-\boldsymbol{y})\phi(\boldsymbol{y},t)\,d\boldsymbol{y}, \end{aligned}$$

where $\phi(\boldsymbol{y},t)$ is the prescribed flux of pathogens from outside. In this study, we supposed $\phi(\boldsymbol{y},t)=0$, which means that there is no external influence on the diffusion in $\Omega$ (Jane White and Gilligan, 2006). The dispersion is forced to act only in $\Omega$ with no interchange of mass between $\Omega$ and the exterior $\mathbb{R}^2\setminus\Omega$ (Andreu-Vaillo et al., 2010, Chapter 3).

The density of spore dispersal $J$ can be computed according to the motion of biological organisms using a stochastic velocity-jump process (Othmer et al., 1988). The spore, which is dispersed by wind, travels with velocity $v_1$ in the $x_1$-direction and velocity $v_2$ in the $x_2$-direction. We denote by $\gamma$ the scattering frequency, that is the homogeneous probability per unit time for wind changing directions. The new wind direction vector $\boldsymbol{v}=(v_1,v_2)$ is randomly chosen from a distribution $q(\boldsymbol{v})$. The spore dispersal process is governed by the linear transport equation which arises when the movement of biological organisms is modeled by velocity-jump process (Othmer et al., 1988)

$$\frac{\partial p}{\partial t}(\boldsymbol{x},t,\boldsymbol{v}) = -\boldsymbol{v}\cdot\nabla p-(\gamma+\mu)p+\gamma q(\boldsymbol{v})\int_{\mathbb{R}^2} p(\boldsymbol{x},t,\boldsymbol{z})\,d\boldsymbol{z},$$

where $p(\boldsymbol{x},t,\boldsymbol{v})$ is the probability density of finding the spore particle at site $x$ and time $t$ moving with velocity $\mathbf{v}$. The spore dispersal density $J$ is given by

$$J(\boldsymbol{x}) = \mu\int_0^{+\infty} e^{-\mu t} p(\boldsymbol{x},t,\boldsymbol{v})\,dt. \tag{9}$$

Indeed, $J$ is the density of spore deposition probability at distance $|\boldsymbol{x}|$ from the origin when released with velocity $\boldsymbol{v}$. Assuming $q$ to be homogeneously distributed on the circle of radius $\nu=|\boldsymbol{v}|$, $p$ is computed using Laplace–Fourier transforms (van den Bosch et al., 1999). According to van den Bosch et al. (1999), when the average flight duration $1/\mu$ is very small compared to the average duration of the air flow in a fixed direction $1/\gamma$, the spore-dispersal distribution $J$ is approximated by the exponential distribution

$$J(x) = \frac{\mu^2}{2\pi\nu^2}\exp\left(-\frac{\mu}{\nu}|x|\right),$$

and when the average time length during which a spore is airborne, $1/\mu$ is very large compared to the average duration of traveling in a fixed direction $1/\gamma$, the spore-dispersal distribution $J$ is approximated as

$$J(x) = \frac{\mu^2}{8\pi\nu^2} K_0\left(\frac{\mu}{\nu\sqrt{2}}|x|\right),$$

where $K_0$ is the zero-order modified Bessel function of the second kind.

Assuming that the diseased leaf area includes the combined densities of latent and symptomatic leaves, the disease severity (expressed in %) at position $\boldsymbol{x}$ and time $t$ can be calculated as follows (Kirtphaiboon et al., 2021):

$$\mathcal{V}(\boldsymbol{x},t) = \frac{E(\boldsymbol{x},t) + I(\boldsymbol{x},t)}{S(\boldsymbol{x},t) + E(\boldsymbol{x},t) + I(\boldsymbol{x},t) + R(\boldsymbol{x},t)} \times 100. \tag{10}$$

### 2.3. Well-posedness of the epidemic

An epidemic model is considered mathematically and biologically well-posed if it admits a unique, positive, and bounded solution. The existence and uniqueness of the solution of the model described by Eq. $((2)_{1-4})$ is highly conditioned by the existence and uniqueness of a solution $u$ to Eq. $(2)_5$ under the initial condition given in Eq. $(3)_3$ which can be derived using the standard Banach fixed point theorem.

Let $t_0 > 0$ and consider the Banach space $W_{t_0} = C\left([0,t_0]; L^1(\Omega)\right)$ endowed with the norm $\|w\|_{W_{t_0}} = \max_{0\le t\le t_0}\{\|w_t\|_{L^1(\Omega)}\}$. The set

$$W_{t_0}^+ = \left\{ w \in W_{t_0} \mid 0 \le w \le 1 \text{ in } \Omega\times(0,+\infty) \right\},$$

is closed in $W_{t_0}$, where $L^1(\Omega)$ is the Lebesgue space of absolutely integrable functions over the domain $\Omega$. For every function $w_0 \in L^1(\Omega)$ satisfying $0 \le w_0 \le 1$ in $\Omega$, we define the nonlinear mapping $\mathcal{T}_{w_0}$ on $W_{t_0}$ as

$$\begin{aligned}\mathcal{T}_{w_0}(w)(\boldsymbol{x},t) = w_0(\boldsymbol{x}) &+ \int_0^t \int_\Omega J(\boldsymbol{x}-\boldsymbol{y})(w(\boldsymbol{y},s) - w(\boldsymbol{x},s))\,d\boldsymbol{y}ds \\ &+ \int_0^t f(w(\boldsymbol{x},s))\,ds.\end{aligned}$$

The solution is obtained as a fixed point of the mapping $\mathcal{T}_{w_0} : W_{t_0} \to W_{t_0}$. We have the following Lemma:

**Lemma 1.** *Let $w_0$ and $z_0$ be functions of $L^1(\Omega)$ satisfying $0 \le w_0, z_0 \le 1$ in $\Omega$. For every $w, z \in W_{t_0}^+$, there exists a constant $C(t_0, J, \Omega)$ such that*

$$\left\|\mathcal{T}_{w_0}(w) - \mathcal{T}_{z_0}(z)\right\|_{W_{t_0}} \le \|w_0 - z_0\|_{L^1(\Omega)} + C(t_0, J, \Omega)\|w - z\|_{W_{t_0}}.$$

**Proof.** The proof follows the same approach as that of Lemma 1 in El Jarroudi et al. (2020). □

**Theorem 2.** *Let $u_0 \in L^1(\Omega)$ such that $0 \le u_0 \le 1$ in $\Omega$. Then the problem (2)–(3) admits a unique non-negative bounded solution such that*

1. $u \in C\left([0,+\infty); L^1(\Omega)\right)$, $0 \le u \le 1$.
2. *$u$ satisfies*

$$\int_\Omega u(x,t)\,dx = \int_\Omega u_0(x)\,dx + \int_\Omega \int_0^t f(u(x,s))\,ds dx. \tag{11}$$

**Proof.**

1. With $w_0 = u_0$ and $z_0 = 0$ in Lemma 1,

$$\left\|\mathcal{T}_{u_0}(u)\right\|_{W_{t_0}} \le C\|u\|_{W_{t_0}} + \|u_0\|_{L^1(\Omega)},$$

therefore, $\mathcal{T}_{u_0}(u) \in W_{t_0}^+$, for $t_0$ small enough.
Consider $w_0 = z_0 = u_0$ in Lemma 1, it is proven that if $t_0$ is chosen such that $C(t_0, J, \Omega) < 1$, then $\mathcal{T}$ is a strict contraction in $W_{t_0}^+$ and the existence and uniqueness part of the theorem follows from Banach's fixed point theorem in the interval $[0,t_0]$. To extend the solution to $[0,\infty)$ one can take $u(x,t_0) \in L^1(\Omega)$ for the initial datum and obtain a solution in $[t_0, 2t_0]$. Iterating this procedure a solution defined in $[0,\infty)$ is thus obtained.
The existence and uniqueness of a solution of the compartmental model Eqs. $(2)_{1,2,3,4}$–$(3)_{1,2}$ is directly deduced from the existence and uniqueness of the solution $u$ of Eqs. $(2)_5$ $(3)_3$ and its boundedness results given the total plant population density in $\Omega$ is constant $(S+E+I+R)(\boldsymbol{x},t) = 1$.

2. Integrating Eq. $(2)_5$ over $\Omega$ and using the Fubini's theorem,

$$\begin{aligned}\int_\Omega \frac{\partial u}{\partial t}(\boldsymbol{x},t)\,d\boldsymbol{x} &= \int_\Omega\int_\Omega J(\boldsymbol{x}-\boldsymbol{y})(u(\boldsymbol{y},t) - u(\boldsymbol{x},t))\,d\boldsymbol{x}d\boldsymbol{y} \\ &\quad + \int_\Omega f(u(\boldsymbol{x},t))\,d\boldsymbol{x}.\end{aligned}$$

As $J$ is symmetric, the first term of the right-hand side cancels. The equality (11) is then obtained when integrating the preceding equality with respect to the time parameter. □

**Remark 2.** According to Legg (1983) most spores do not disperse beyond the originating crop field; instead, they are typically deposited on other plants within the same field or fall onto the ground within a few meters of their point of release. Identity (11) which means that, at any time $t > 0$, the total number of fungal spores in the field is the sum of the initial number of fungal spores present in the field and the number of fungal spores produced by all infected hosts in the field according to time since infection, shows that, in accordance with Legg (1983), the spore dispersion occurs mainly within the field.

**Corollary 1** (*Final Size of the Epidemic*). *Let $S_\infty(\boldsymbol{x}) := \lim_{t\to\infty} S(\boldsymbol{x},t)$ be the density of healthy individual plants at the final level at the site $\boldsymbol{x}$ and $u_\infty(\boldsymbol{x}) := \lim_{t\to\infty} u(\boldsymbol{x},t)$ be the density of fungal pathogens at the final level at the site $\boldsymbol{x}$. The final disease level in the field is described by the following identity:*

$$\begin{aligned}\int_\Omega u_\infty(\boldsymbol{x})\,d\boldsymbol{x} &= \int_\Omega u_0(\boldsymbol{x})\,d\boldsymbol{x} \\ &\quad + \kappa\int_\Omega \left(S_0(\boldsymbol{x}) - S_\infty(\boldsymbol{x})\right)d\boldsymbol{x}.\end{aligned} \tag{12}$$

**Proof.** using Eq. (5), we have

$$\begin{aligned}\int_\Omega\int_0^t f(u(\boldsymbol{x},s))\,ds d\boldsymbol{x} &= \kappa\int_\Omega\int_0^t\int_0^s \alpha(s-\xi)(uS)(\boldsymbol{x},s-\xi)\varpi(\xi)\,d\xi ds d\boldsymbol{x} \\ &= -\kappa\int_\Omega\int_0^t\int_0^s \frac{\partial S}{\partial s}(\boldsymbol{x},s-\xi)\varpi(\xi)\,d\xi ds d\boldsymbol{x} \\ &= -\kappa\int_\Omega\int_0^t \frac{\partial}{\partial s}\left(\left(S(\boldsymbol{x},.) - S_0(\boldsymbol{x})\right) * \varpi\right)(s)\,ds d\boldsymbol{x} \\ &= -\kappa\int_\Omega \left(\left(S(\boldsymbol{x},.) - S_0(\boldsymbol{x})\right) * \varpi\right)(t)\,d\boldsymbol{x}.\end{aligned} \tag{13}$$

Then, substituting in Eq. (11), we deduce that

$$\begin{aligned}\int_\Omega u(\boldsymbol{x},t)\,d\boldsymbol{x} &= \int_\Omega u_0(\boldsymbol{x})\,d\boldsymbol{x} \\ &\quad - \kappa\int_\Omega \left(\left(S(\boldsymbol{x},.) - S_0(\boldsymbol{x})\right) * \varpi\right)(t)\,d\boldsymbol{x},\end{aligned} \tag{14}$$

then, using Lebesgue's dominated convergence theorem, we deduce the identity (Eq. (12)). □

## 3. Numerical applications

### 3.1. Model discretization

In this section, we discretize the nonlocal reaction–diffusion model (2) using uniform grids in space and Euler temporal discretization in time. We consider a two-dimensional spatial domain $\Omega = [0, L_{x_1}] \times [0, L_{x_2}]$ covered with $N_{x_1} \times N_{x_2}$ cells, and a temporal domain $[0,T]$ discretized into $N_t$ steps.

Let $\delta x_1 = L_{x_1}/N_{x_1}$ and $\delta x_2 = L_{x_2}/N_{x_2}$ be the spatial step sizes and $\delta t = T/N_t$ be the time step size. We define the grid points by $x_{1i} = i\delta_{x_1}$, $i = 1, 2, \ldots, N_{x_1}$ and $x_{2j} = j\delta_{x_2}$, $j = 1, 2, \ldots, N_{x_2}$, and $t_n = n\delta_t$, $n = 1, 2, \ldots, N_t$ where the subscript $i$ and $j$ refer to the computational cells and the superscript $n$ is used for the time step. We denote by $\boldsymbol{U}_{i,j}^n$ the approximate value of $\boldsymbol{U}(x_{1i}, x_{2j}, t_n)$ where $\boldsymbol{U} := (u, S, E, I, R)$. Extending the approach developed in El Jarroudi et al. (2020), the convolution product $\int_\Omega J(\boldsymbol{x}-\boldsymbol{y})(u(\boldsymbol{y},t)-u(\boldsymbol{x},t))\,d\boldsymbol{y}$ is approximated based on the rectangle rule for integrals and is given by

$$\left[\int_\Omega J(\boldsymbol{x}-\boldsymbol{y})(u(\boldsymbol{x},t)-u(\boldsymbol{y},t))\,d\boldsymbol{y}\right]_{i,j}^n \simeq \sum_{p=1}^{N_{x_1}}\sum_{l=1}^{N_{x_2}} J\left(x_{1i}-y_{1p}, x_{2j}-y_{2l}\right)\left(u_{i,j}^n - u_{p,l}^n\right) \times \delta x_1 \delta x_2, \tag{15}$$

for every $i = 1, 2, \ldots, N_{x_1}$, $j = 1, 2, \ldots, N_{x_2}$, and $n = 1, 2, \ldots, N_t$.

Likewise, the term $f\left(x_{1i}, x_{2j}, t_n\right) := f_{i,j}^n$ involves a convolution product with respect to the time parameter and can be approximated as follows

$$\begin{aligned} f_{i,j}^n &= \left[\kappa\int_0^t \alpha(s)(uS)(\boldsymbol{x}, t-s)\varpi(s)(s)ds\right]_{i,j}^n \\ &\simeq \kappa\sum_{k=1}^{n}\alpha(t_n - t_k)\varpi\left(t_n - t_k\right)(uS)_{i,j}^k\,\delta t, \end{aligned} \tag{16}$$

The discretized form of the nonlocal reaction–diffusion model (2) is obtained using the Euler temporal discretization. This is given by

$$\begin{cases} S_{i,j}^{n+1} &= \dfrac{S_{i,j}^n}{1+\delta t\alpha^{n+1}u_{i,j}^{n+1}}, \\ E_{i,j}^{n+1} &= \dfrac{E_{i,j}^n + \delta t\alpha^{n+1}u_{i,j}^{n+1}S_{i,j}^{n+1}}{1+\eta^{n+1}\delta t}, \\ I_{i,j}^{n+1} &= \dfrac{I_{i,j}^n + \delta t\eta^{n+1}E_{i,j}^{n+1}}{1+\beta\delta t}, \\ R_{i,j}^{n+1} &= R_{i,j}^n + \delta t\beta I_{i,j}^{n+1}, \\ u_{i,j}^{n+1} &= u_{i,j}^n + \delta t\left(\sum_{p=1}^{N_x}\sum_{l=1}^{N_{x_2}} J\left(x_{1i}-y_{1p}, x_{2j}-y_{2l}\right)\right. \\ &\qquad \left.\times\left(u_{i,j}^n - u_{p,l}^n\right)\delta x_1\delta x_2 + f_{i,j}^n\right), \end{cases} \tag{17}$$

with the following initial condition

$$\begin{cases} S_{i,j}^1 &= S_0(\boldsymbol{x}), \quad E_{i,j}^1 = E_0, \\ I_{i,j}^1 &= I_0(\boldsymbol{x}), \quad R_{i,j}^1 = R_0(\boldsymbol{x}), \\ u_{i,j}^1 &= u_0(\boldsymbol{x}), \end{cases}$$

for every $i = 1, \ldots, N_{x_1}$, $j = 1, \ldots, N_{x_2}$ and $n = 1, \ldots, N_t$.

In this study, the initial condition $u_0(x_1, x_2) = \exp(-0.1(4-x_1)^2 - (0.75-x_2)^2)$ was used for the spore dispersal variable (Jane White and Gilligan, 2006). Due to the lack of data for $S_0$, $E_0$, $I_0$ and $R_0$, we assumed a homogeneous distribution at the starting time. The initial values of the variables $S_0$, $E_0$, $I_0$ and $R_0$ (Table 1) were selected such that the computed disease severity $\mathcal{V}$ as defined in Eq. (10) matched the UAV-derived disease severity estimates at the start of the simulations. Numerical simulations were initiated after the onset of the epidemics, assuming that at time $t = 0$, infectious and removed plants were already present. At this initial simulation time, we assumed that the infectious plants have already completed their latency periods.

**Table 1**
The initial conditions used for the numerical simulations of the SEIR model for WSR (caused by *Puccinia striiformis*) and WLR (caused by *P. triticina*).

| Site | Variable | Wheat stripe rust | Wheat leaf rust |
|---|---|---|---|
| Bettendorf | $S_0$ | 0.8000 | 0.8000 |
| | $E_0$ | 0.0000 | 0.0000 |
| | $I_0$ | 0.0192 | 0.0396 |
| | $R_0$ | 0.1808 | 0.1604 |
| Bicherhaff | $S_0$ | 0.8100 | 0.8000 |
| | $E_0$ | 0.0000 | 0.0000 |
| | $I_0$ | 0.0042 | 0.0045 |
| | $R_0$ | 0.1858 | 0.1819 |
| Koerich | $S_0$ | 0.8000 | 0.8000 |
| | $E_0$ | 0.0000 | 0.0000 |
| | $I_0$ | 0.0215 | 0.0114 |
| | $R_0$ | 0.1785 | 0.1886 |
| Weiswampach | $S_0$ | 0.8000 | 0.8000 |
| | $E_0$ | 0.0000 | 0.0000 |
| | $I_0$ | 0.0147 | 0.0145 |
| | $R_0$ | 0.1853 | 0.1855 |

The disease severity (Eq. (10)) at the discrete level is given by

$$\mathcal{V}_{i,j}^{n+1} = \frac{E_{i,j}^{n+1} + I_{i,j}^{n+1}}{S_{i,j}^{n+1} + E_{i,j}^{n+1} + I_{i,j}^{n+1} + R_{i,j}^{n+1}} \times 100. \tag{18}$$

In our numerical simulations, $\tau$ is computed as the mean value of the latency period LP (Table 2) by $\tau = \sum_{n=1}^{N_t} LP(t^n)/N_t$.

### 3.2. Study sites

The proposed SEIR model (Eqs. (2)–(17)) was employed to analyze the dynamics of WSR and WLR in winter wheat fields located in Bettendorf, Bicherhaff, Koerich, and Weiswampach, in the Grand Duchy of Luxembourg, during the 2018–2019 cropping season (Fig. 1). Fungal disease monitoring at these sites was part of a broader in-season surveillance program conducted in commercial fields, which typically involved various cultivars subjected to different fungicide regimes, ranging from zero to three applications (Heidarian Dehkordi et al., 2020a).

The experimental design was a complete randomized block with four replicates at Bettendorf and three replicates at Bicherhaff, Koerich, and Weiswampach (one plot = 12 $m^2$ (8 m × 1.5 m)) (Heidarian Dehkordi et al., 2020a). Wheat was typically sown in October and harvested in July or August of the following year. The wheat variety 'Kerubino', which is moderately susceptible to both WSR and WLR (BSA, 2018), was cultivated at all sites. At Bettendorf an additional variety, 'Desamo', noted for its resistance (i.e., lower susceptibility) to both diseases, was also grown (BSA, 2018). Consequently, 12 plots were monitored at Bicherhaff, Koerich, and Weiswampach, while 32 plots were monitored at Bettendorf. All plots received three applications of ammonium nitrate fertilizer: 40–70 kg N $ha^{-1}$ at tillering (growth stage 25), 60–70 kg N $ha^{-1}$ at stem elongation (growth stage 32), and 65–95 kg N $ha^{-1}$ around ear emergence completion (growth stage 59). All plots were maintained weed free throughout the season.

Several fungal diseases were recorded at the study sites during the monitoring period. Visual assessments of disease severity were conducted weekly from April to July 2019 on the leaves of selected plants (10 plants per plot) that were marked at the start of the monitoring period. Disease severity was expressed as the percentage of leaf area diseased. The main diseases included Septoria tritici blotch (caused by *Zymoseptoria tritici* (Desm.) Quaedvlieg & Crous), WSR, WLR, powdery mildew (caused by *Blumeria graminis* DC. f. sp. *tritici em.* Marchal), and *Fusarium* head blight (caused by a complex of *Fusarium graminearum* Schwabe and *Fusarium culmorum*). Given that the pathogens of WSR and WLR are obligate biotrophs (i.e., they require living host tissue

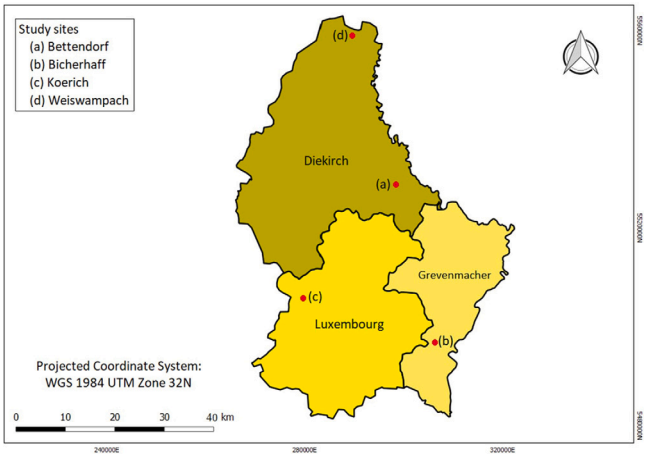


**Fig. 1.** Location of the study sites in the Grand Duchy of Luxembourg.

to complete their life cycle), no visual assessments of WSR and WLR were conducted on senesced leaves. Data from the visual disease severity assessment were used for evaluating the performance of severity estimates from UAV imagery (see Section 3.4 and Heidarian Dehkordi et al. (2020a)).

### 3.3. Meteorological data

Hourly air temperature and relative air humidity data for the period of March to July 2019 for each site were used. Data were recorded at an automatic weather station located within 1 to 2 km of each experimental field. Warm and relatively dry conditions were observed generally during June and July at all sites (Fig. 2). Daily mean temperatures varied between 4 °C and 28 °C during the study period, with averages of 13 °C at Bettendorf and Bicherhaff, 12 °C at Koerich, and 11 °C at Weiswampach (Fig. 2). The average relative air humidity at the study sites was above 74% (range = 58–97%), with highest values recorded at Weiswampach.

### 3.4. UAV imagery derived disease severity estimates

Unmanned aerial vehicle (UAV) imagery was captured on four dates, May 15, May 24, June 5, and July 3, 2019, at each of the study sites. A DJI Phantom 4 Pro quadcopter (DJI, Nanshan, Shenzhen, China) equipped with a built-in 20 MP Red-Green-Blue (RGB) sensor and an 84° field of view was used for image acquisition. Flights were conducted at an altitude of 10 m above ground level and a nominal speed of 4 m $s^{-1}$, with 85% front lap and 75% side lap parallel-axis flight lines. This configuration resulted in RGB images with a ground sampling distance of 0.28 cm. Image processing was performed using the Pix4Dmapper photogrammetric software (Pix4D S.A., Lausanne, Switzerland). First, point clouds and mesh surface models were generated via aerial triangulation. Subsequently, high-resolution RGB orthomosaics were produced through image orthorectification (Heidarian Dehkordi et al., 2020b). From the resultant orthomosaics canopy cover values were estimated as follows:

$$\lambda_1 = DN_{\text{Green}} - DN_{\text{Blue}} \quad \textit{and} \quad \lambda_2 = DN_{\text{Green}} - DN_{\text{Red}} \tag{19}$$

where $DN_{\text{Green}}$, $DN_{\text{Blue}}$, and $DN_{\text{Red}}$ are the digital numbers (DNs) of the green, blue and red channels of the visible spectrum, respectively. Values above 20 for both $\lambda_1$ and $\lambda_2$ were chosen because they allowed for a better characterization of canopy cover when comparing visually the preliminary estimates against corresponding RGB images (Heidarian Dehkordi et al., 2020a).

Soil background effects were removed by applying the computed vegetation mask (Eq. (19)). Wheat leaves infected by WSR were identified using the WSR index (WSRI), calculated as follows (Heidarian Dehkordi et al., 2020a).

$$WSRI = \left[(DN_{\text{Green}} + DN_{\text{Red}})\right] > \lambda_2 \tag{20}$$

Similarly, leaves infected by WLR were identified using the WLR index (WLRI), calculated as follows (Heidarian Dehkordi et al., 2020a).

$$WLRI = \left[\left(\frac{2 \times DN_{\text{Green}} - DN_{\text{Red}}}{2 \times DN_{\text{Red}} + 2 \times DN_{\text{Green}} - DN_{\text{Blue}}}\right)\right] < \lambda_1 \tag{21}$$

A visual cryptography technique was employed to differentiate leaf areas affected by WSR and WLR (Heidarian Dehkordi et al., 2020a; Heidarian Dehkordi et al., 2020b). For WSR, the pixel values of the resulting virtual raster image ranged from 0 DN to 500 DN, while for WLR, Eq. (21) resulted in a virtual raster image with pixel values ranging from 0 DN to 1 DN. Preliminary threshold estimates for WSRI and WLRI were visually compared against the corresponding RGB images. The boundaries of computed WSR- and WLR-infected leaf areas, as detected using Eqs. (20) and (21), respectively, were overlaid to compute the difference in area. Based on this analysis, the thresholds that resulted in the most accurate classification (i.e., small classification errors) were determined to be $\lambda_2 = 400$ for WSR and $\lambda_1 = 0.3$ for WLR (Heidarian Dehkordi et al., 2020a). Accordingly, all pixel values above 400 (for WSR) and 0.3 (for WLR) were discarded as non-infected areas. Subsequently, all pixels corresponding to WSR and WLR-infected leaves were converted into polygon shapefiles, and the respective total areas were computed. Image processing and analysis were conducted using Pix4Dmapper photogrammetric software (Pix4D S.A., Lausanne, Switzerland) and the Quantum Geographic Information System (QGIS) software (Open Source Geospatial Foundation, Chicago, IL, USA).

Comparisons between observed disease severity and values derived from UAV imagery were evaluated using correlation analysis. Statistical significance was assessed with the non-parametric Kendall's rank correlation coefficient. A detailed description of the UAV data processing and comparison results can be found in Heidarian Dehkordi et al. (2020a).

### 3.5. Estimation of model parameters and fitting quality

Table 2 provides the values of parameters used in our numerical simulations. The parameters $n$, $m$, and $d$, which are related to spore dispersal probability (Eq. (4)), were fitted from the SEIR model by minimizing the error, i.e., the root mean square error (RMSE), between the field data (UAV imagery derived) from Heidarian Dehkordi et al. (2020a) and model-estimated disease severity. Initial parameter values were set based on the literature (e.g., van den Bosch et al., 1988; Hau and de Vallavieille-Pope, 2006; El Jarroudi et al., 2020). The SEIR model was then run and data pairs (UAV imagery derived vs. model estimates) were compared for each case study. The set of parameter values resulting in the smallest RMSE was kept. Consequently, the values for $n$, $m$, and $d$ varied according to the site and the disease (Table 2). The remaining parameters were derived from the literature (de Vallavieille-Pope et al., 2002; El Jarroudi et al., 2020; Sinha and Chen, 2021); their values remained constant for all sites (Table 2).

The spatiotemporal dynamics of spore dispersal u and those of susceptible S, exposed $E$, infectious $I$, and removed $R$ individuals for WSR and WLR were computed for the period of May to July 2019. Numerical simulations were performed to explore the impact of different model parameters, initial and boundary conditions on the evolution of WSR and WLR at the study sites. The solution $u$, $S$, $E$, $I$ and $R$ for the problem (2)–(3) is presented along the $-x_1$ direction of the space (Figs. 3, 4, 5, 6 and 7, and 8). We further compared the mean values of WSR and WLR severities over the computational domain predicted by the SEIR model using Eq. (18) against the values estimated from UAV imagery (Fig. 9). The quality of the model fit in simulating disease severity was assessed using the RMSE and the mean absolute percentage error (MAPE) as shown in Table 3. Finally, simulations of disease severity for WLR and WSR across three dates (May 24, June 5, and July 3) are presented in a two-dimensional space (Fig. 10).

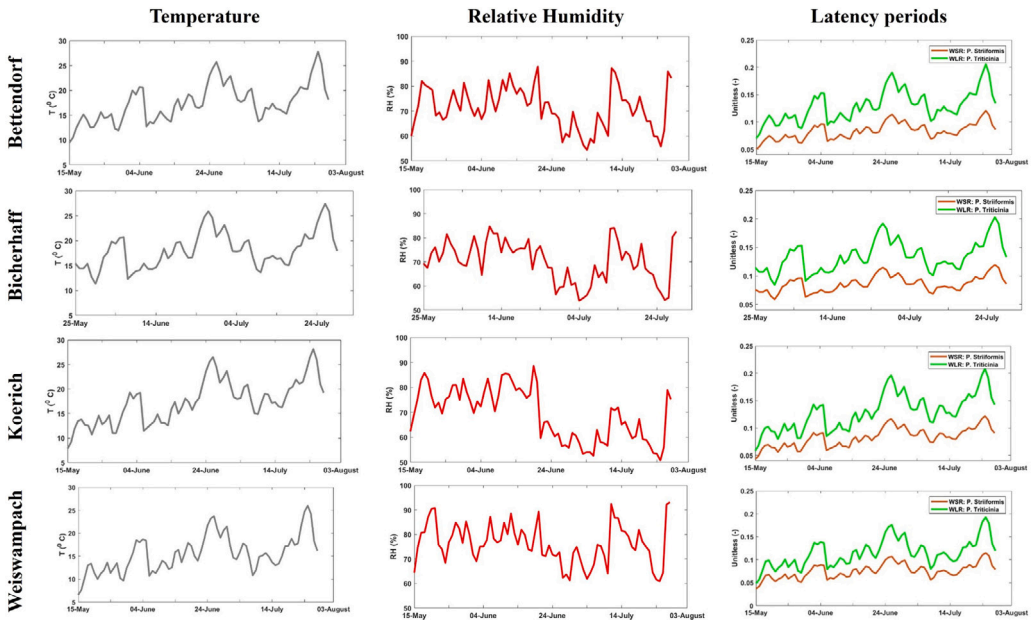


**Fig. 2.** Variations of mean air temperature (left), relative air humidity (middle), and simulated latency periods (right) at the study sites during March-July 2019. Latency periods for WSR (green curve) and WLR (brown curve) were calculated using equations from Eversmeyer et al. (1988), El Jarroudi et al. (2014), Zadoks (1971) and El Jarroudi et al. (2017), respectively (Table 2).

**Table 2**
Values of parameters used in the numerical applications.

| Site | Parameter[a] | Values | | Source(s) |
|---|---|---|---|---|
| | | Whet stripe rust | Wheat leaf rust | |
| All | $\kappa$ | $45.10^4$ | $40.10^3$ | Papastamati and van den Bosch (2007), Eversmeyer and Kramer (2000) and El Jarroudi et al. (2020) |
| | $\nu$ | 1.5 | 1 | idem |
| | $\frac{\nu}{\mu}$ | 3.29 | 2.19 | idem |
| | $\beta$ | 0.033 | 0.05 | idem |
| | $a$ | 0.20 | 0.24 | idem |
| | $b$ | 3.00 | 2.86 | idem |
| | $W_{\min}$ | 32 | 20 | Eversmeyer et al. (1988) and de Vallavieille-Pope et al. (1995); |
| | $\Phi_{\max}$ | 0.421 | 0.435 | de Vallavieille-Pope et al. (2002) |
| | $LP$ | $\frac{1005 + 11.3T(t)}{2.5 + 5.65T(t)}$ | $\frac{1}{0.00741T(t)}$ | Zadoks (1971) and El Jarroudi et al. (2017) |
| | | | | Eversmeyer et al. (1988) and El Jarroudi et al. (2014) |
| Bettendorf | $n$ | 3.5 | 9.5 | |
| | $m$ | 1 | 1.73 | Fitted from the model (this study) |
| | $d$ | 0.00164 | 0.5 | |
| Bicherhaff | $n$ | 0.18 | 2 | |
| | $m$ | 7.8 | 0.4 | Fitted from the model (this study) |
| | $d$ | 0.032 | 0.0036 | |
| Koerich | $n$ | 0.74 | 5 | |
| | $m$ | 0.11 | 5 | Fitted from the model (this study) |
| | $d$ | 0.00072 | 0.0012 | |
| Weiswampach | $n$ | 0.1 | 0.6 | |
| | $m$ | 0.8 | 5 | Fitted from the model (this study) |
| | $d$ | 0.00043 | 0.0021 | |

[a] $\kappa$: average number of pathogen particles produced per host infected; $\frac{\nu}{\mu}$: wind velocity component; $\beta$: homogeneous probability per unit time that an individual reaches the end of the infectious period; $a$ and $b$: shape parameters of the sporulation curve; $LP$: latency period; $W_{\min}$: minimum wetness period for infection; $\Phi_{\max}$: maximum infection efficiency; $n$, $m$ and $d$: shape parameters of the spore dispersal curve.

### 3.6. Simulated spatiotemporal patterns of spore dispersals

Fig. 3 presents the cross-section view along the $x_1$-axis of the simulated spatiotemporal patterns of spore dispersal $u$. Both pathogens exhibited spatial and temporal variation in spore dispersal density across the study sites. For WSR, the spore dispersal density fluctuated with distance at all locations, showing localized and sustained peaks during May and June (indicated by red zones in Fig. 3), followed by a sharp decline in late June and July. A gradual dissipation in density was observed with increasing distance from the source. For WLR, similar patterns were observed at Bicherhaff, Koerich, and Weiswampach. However, at Bettendorf, the model simulated low spore densities in May and June, which then increased and peaked in late June before declining (Fig. 3). It is important to note that the initial

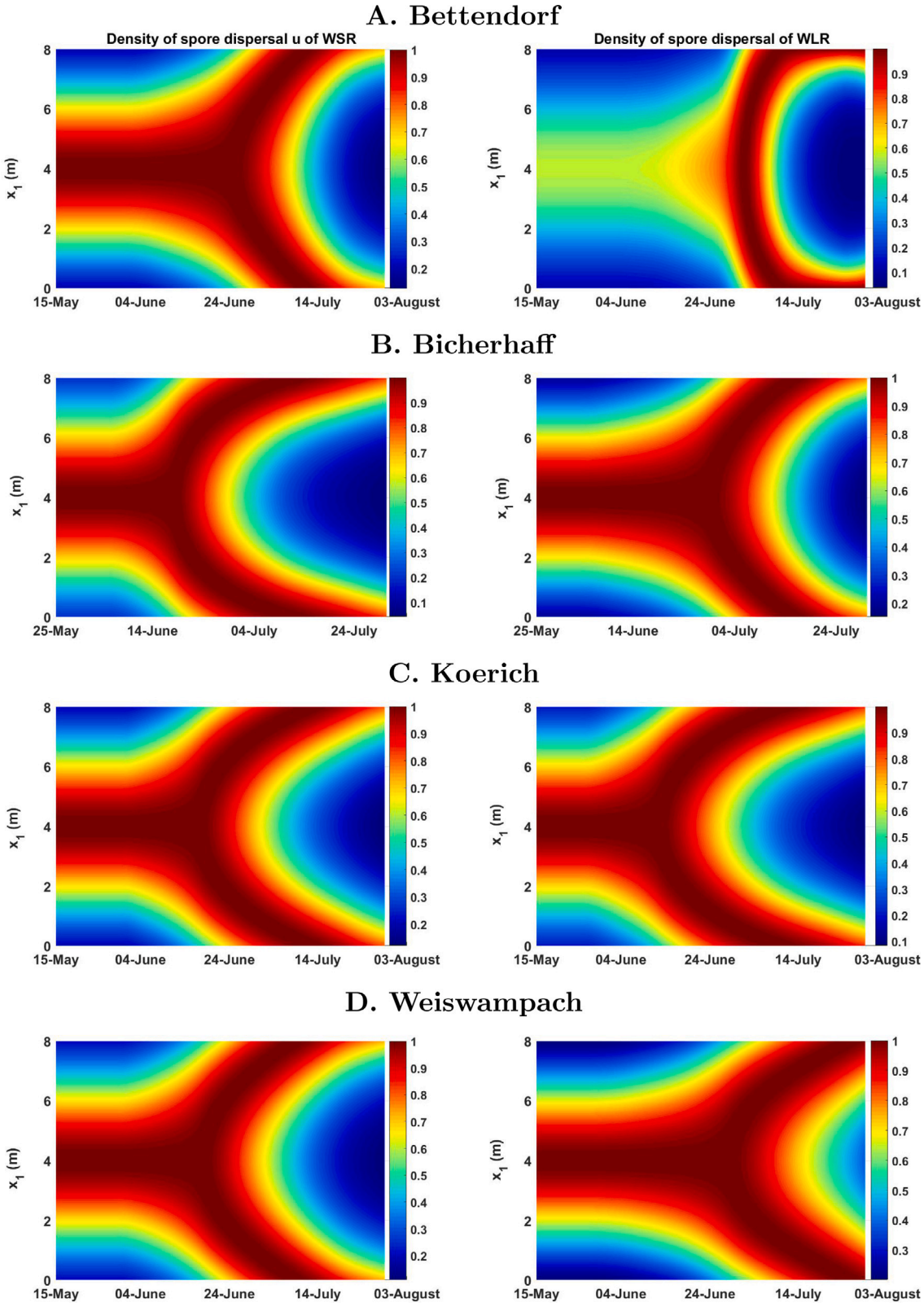


**Fig. 3.** Simulated spore dispersal density u of WSR (left) and WLR (right) across four locations: Bettendorf (A), Bicherhaff (B), Koerich (C), and Weiswampach (D), shown as a cross-section along the $x_1$-axis between May and July 2019.

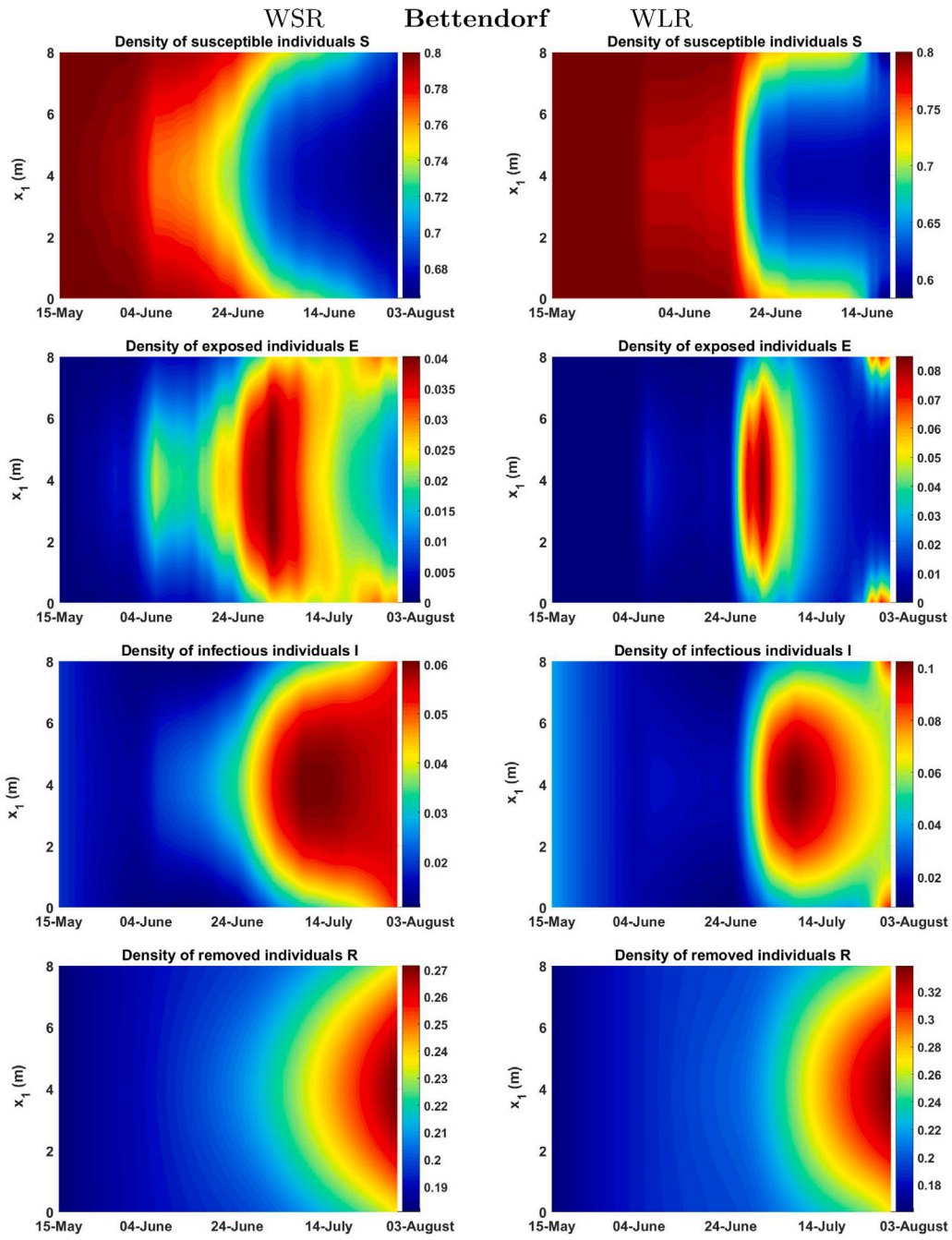


**Fig. 4.** Simulated $S$, $E$, $I$ and $R$ compartments of WSR (left) and WLR (right) at Bettendorf, shown as a cross-section along the $x_1$-axis between May and July 2019.

spore loads and wind velocity and direction were not measured at the study sites. Incorporating such observations would help improve model parameterization and enhance the model's performance.

### *3.7. Simulated spatiotemporal patterns of individuals in the SEIR compartments*

The cross-section along the $x_1$-axis for the simulated spatiotemporal distributions of $S$, $E$, $I$, and $R$ individuals for WLR and WSR at the study sites are presented in Figs. 4–7. For the $E$ compartment, the number of peaks and dates of occurrence simulated by the model in both disease cases varied across sites (Figs. 4–7, second ligne). In Bettendorf one peak was simulated by the model in each disease case approximately at the same time by early July (Figs. 4–7). For the remaining sites, multiple peaks were simulated. For example, for WSR at Koerich (Fig. 7 (left)), the first peak in the $E$ compartment occurred around mid-June, with a sharp rise and subsequent decline, likely corresponding to the primary infection cycle. The second peak emerged around mid-July, suggesting either a secondary infection wave or delayed interactions between environmental factors and host susceptibility.

For the $I$ compartment, the simulations showed a clear temporal evolution of the density of infectious plants with localized hotspots for both diseases at all sites (Figs. 4–7). Among all sites, Koerich showed a sustained high density of infectious plants for both diseases compared to other sites, with areas of high density persisting for a longer duration between late June and July (Fig. 6). Similar pattern was simulated for WSR in Bettendorf (Fig. 4 (left)), indicating the potential vulnerability of these sites to disease outbreaks– WLR and WSR for Koerich and

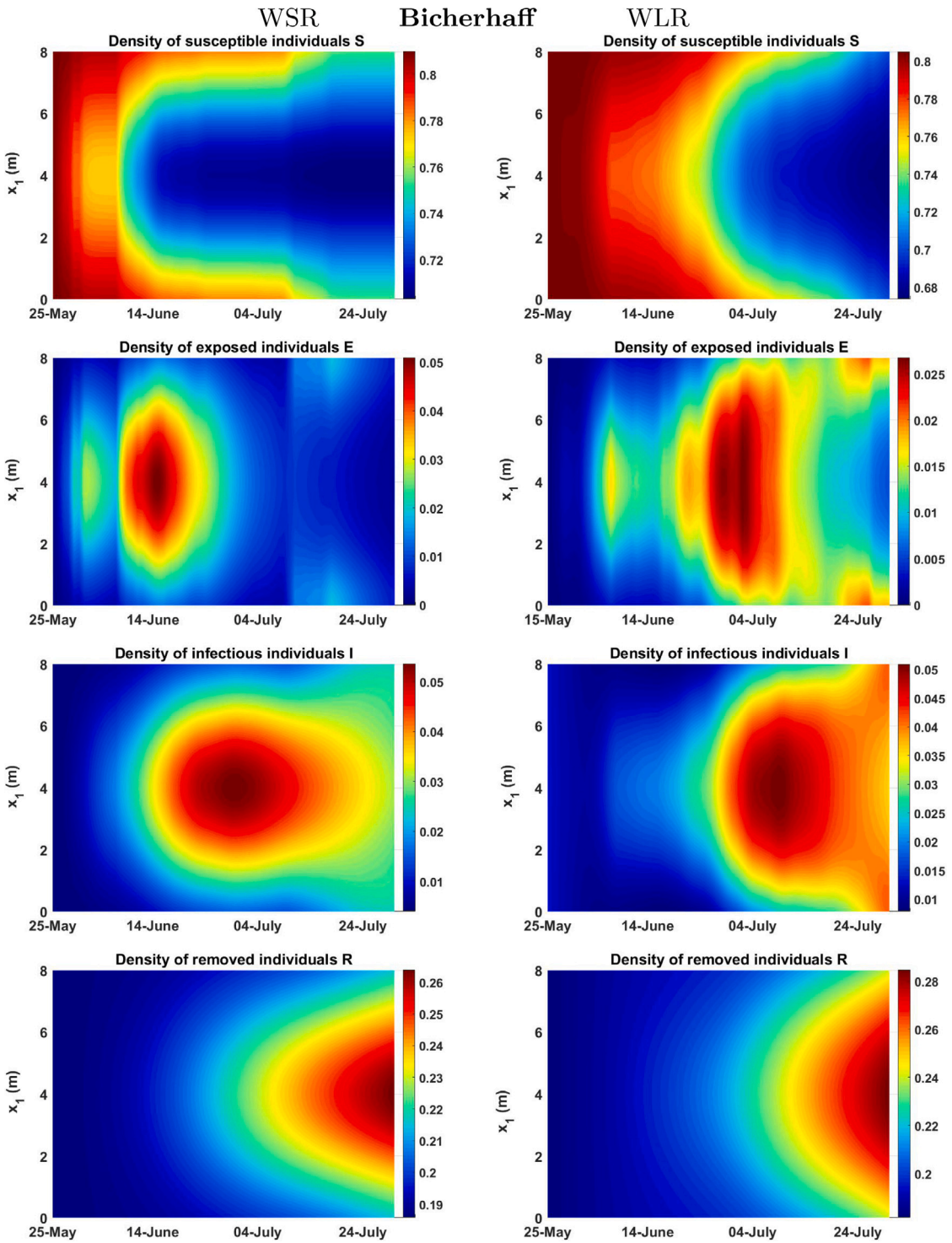


**Fig. 5.** Simulated $S$, $E$, $I$ and $R$ compartments of WSR (left) and WLR (right) at Bicherhaff, shown as a cross-section along the $x_1$-axis between May and July 2019.

WSR for Bettendorf. The simulated onset of sustained high density of infectious plants at these two sites highlight a critical period for disease management efforts, namely for proactive strategies to limit the disease spread and mitigate its impact on yield.

### 3.8. SEIR-based WSR and WLR severity estimates

Fig. 8 shows the cross-section along the $x_1$-axis for the simulated rust severity percentages (%) over time. Both diseases showed non-uniform spatial distribution, with localized hotspots shifting across the $x_1$- axis, suggesting spatial progression of the diseases (Fig. 8). The simulated WSR severity density showed slightly more localized peaks over time, while WLR often exhibited a broader spatial spread. The severity of both diseases most often peaked around late June to mid-July, aligning with seasonal factors conducive to disease development (e.g., temperature and humidity). Bettendorf and Bicherhaff showed more pronounced peaks, while Koerich and Weiswampach exhibited more moderate but sustained severity levels (Fig. 8). For instance, at Bicherhaff two distinct peaks were visible for WLR, one in early June

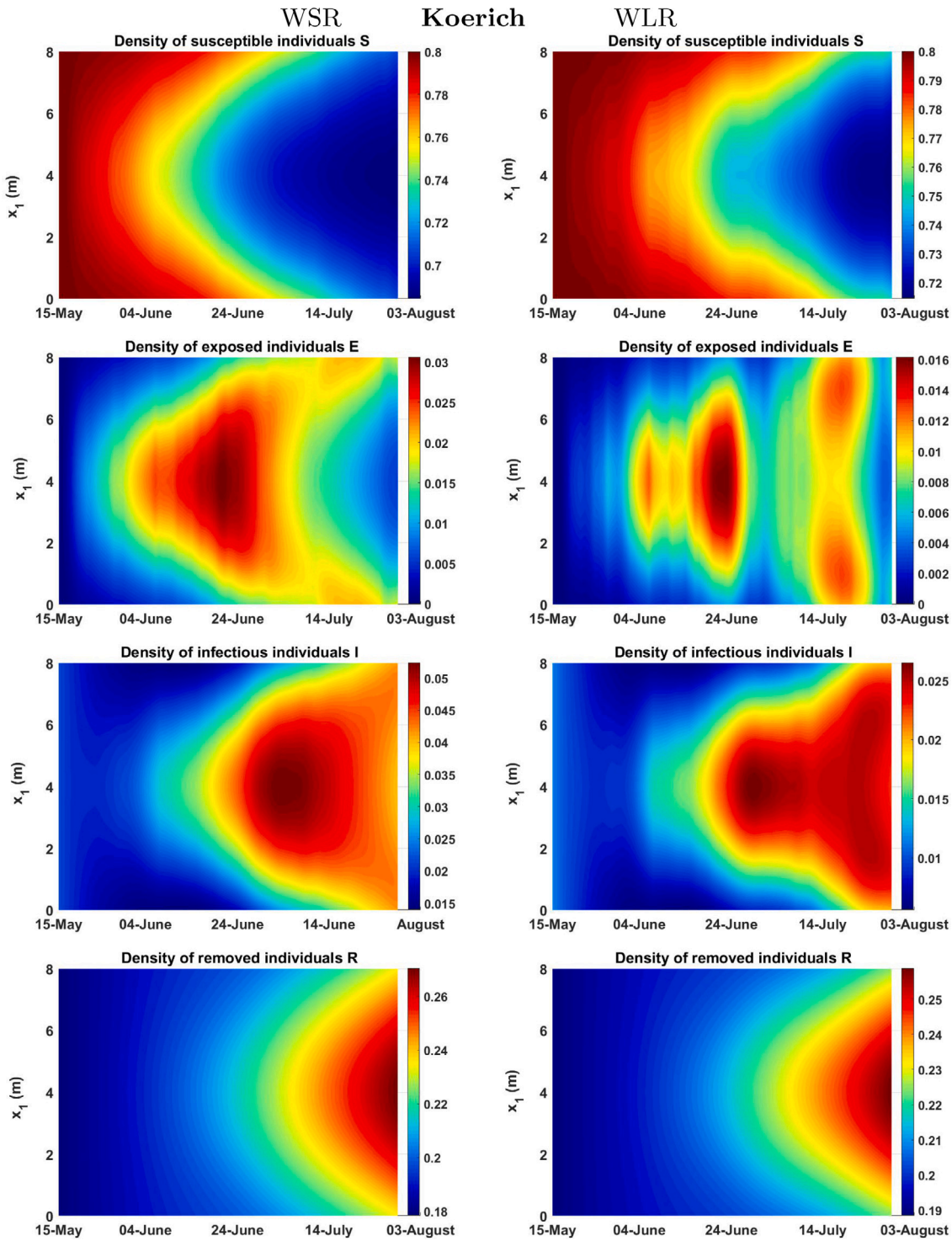


**Fig. 6.** Simulated $S$, $E$, $I$ and $R$ compartments of WSR (left) and WLR (right) at Koerich, shown as a cross-section along the $x_1$-axis between May and July 2019.

and the second in early July, suggesting multiple infection cycles. The severity was moderate but sustained over time, with high values spread evenly across the spatial domain (Fig. 8B, left insert). This pattern indicates favorable conditions for WLR throughout the observation period. With regard to WSR, its severity at Bicherhaff followed a steady increase, peaking slightly later than WLR in mid-July. The peak severity was lower, and its spatial distribution appeared more patchy, suggesting localized susceptibility or environmental constraints limiting its spread (Fig. 8B, right insert). At Koerich (Fig. 8C), WLR severity rose sharply in early June and sustained relatively high levels until early July. The spatial distribution was broad, with consistently high severity across the field, indicating uniform conducive environmental conditions or host susceptibility. Whereas WSR severity remained moderate at the beginning of the monitoring and increased steadily through mid-July, with a later peak than WLR. Similar to Weiswampach, the noticeable spatial heterogeneity, with localized areas of higher severity (Fig. 8C and D, right insert), might be explained by microclimatic differences or spatially variable host conditions. The gradual decline in infected plant density towards the end of the season suggests a depletion of susceptible hosts, potentially due to environmental changes

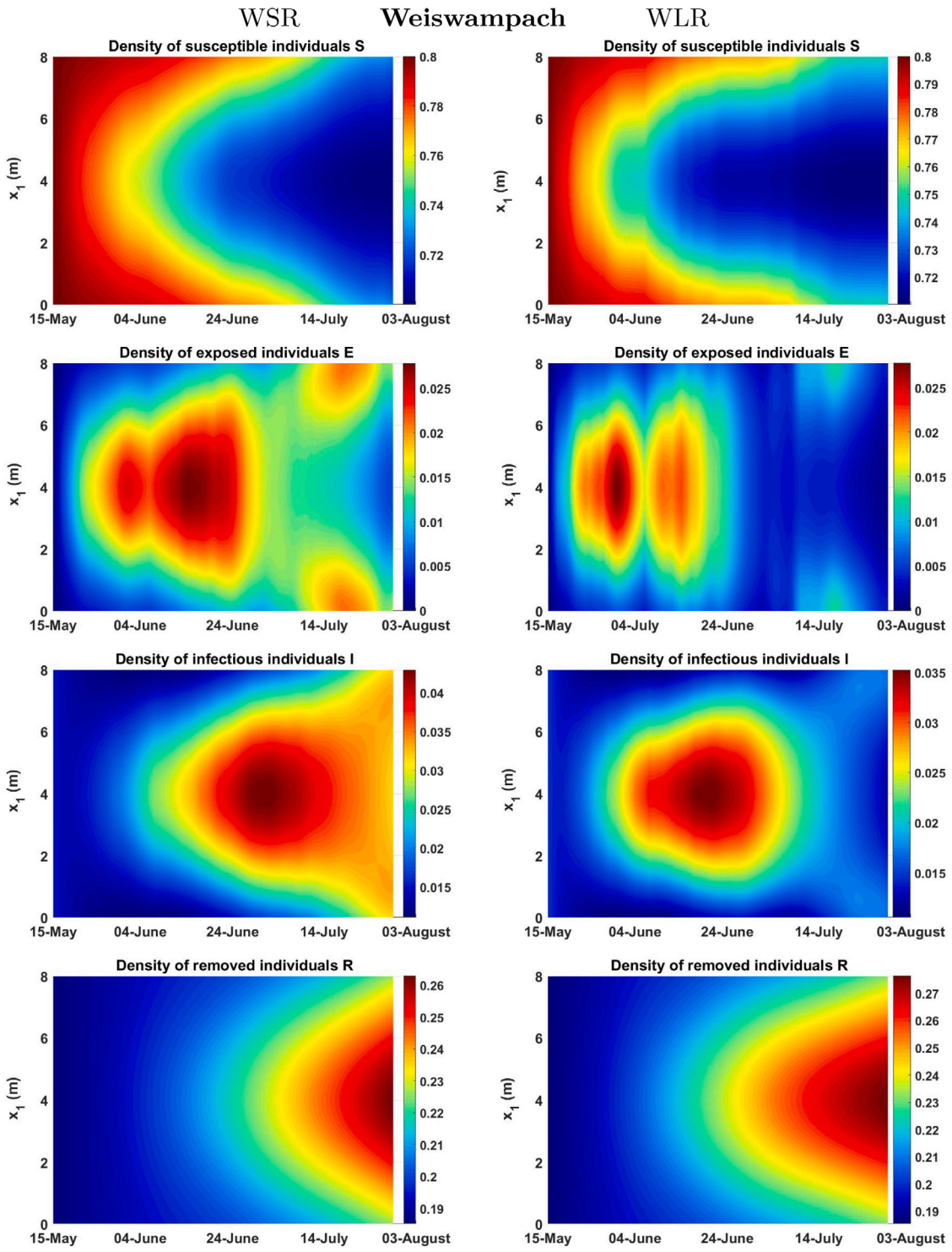


**Fig. 7.** Simulated $S$, $E$, $I$, and $R$ compartments of WSR (left) and WLR (right) at Weiswampach, shown as a cross-section along the $x_1$-axis between May and July 2019.

and/or leaves senescence. Both *P. striiformis* and *P. triticina* are obligate biotrophic pathogens. Towards the end of the cropping season, leaves will senesce, limiting the development of both diseases.

### *3.9. Comparisons between UAV imagery derived and SEIR-based WLR and WSR severity estimates*

Fig. 9 presents the simulated SEIR-based disease severities compared to UAV imagery-derived values (Heidarian Dehkordi et al., 2020a) for both WSR and WLR across the study sites, including Bettendorf and Weiswampach, Bicherhaff, and Koerich. Overall, the results show a good fit of the SEIR model in simulating disease severities, as confirmed by the MAPE and RMSE values (Table 3). At the site level, the lowest errors for WSR were obtained in Weiswampach and Koerich, with MAPE values of 3% and 5% and RMSE values of 0.14 and 0.16 percentage points, respectively (Table 3). For WLR, Weiswampach exhibited the lowest error, with a MAPE of 10% and an RMSE of 0.55 percentage points. The highest error for WSR was found at Bicherhaff,

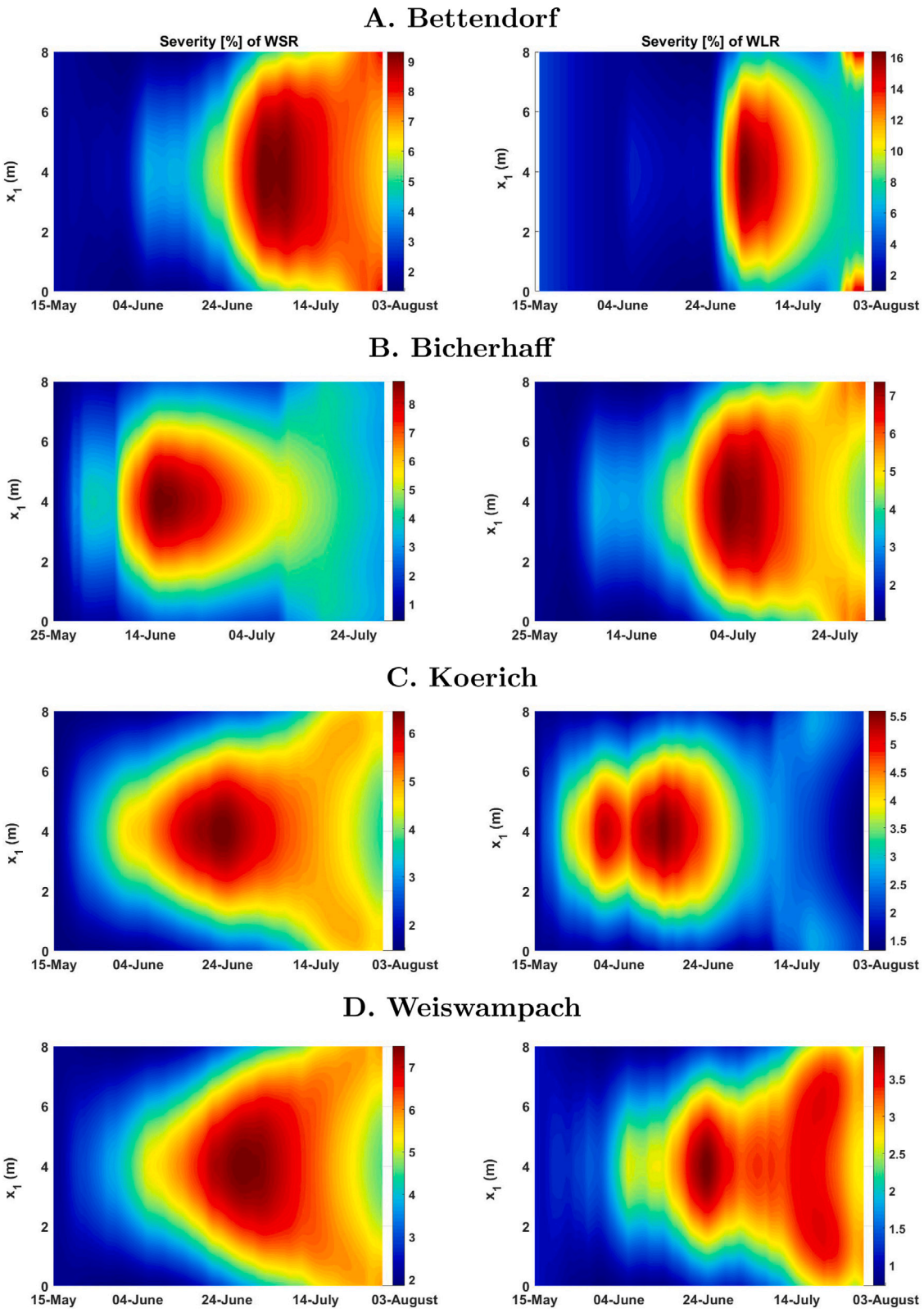


**Fig. 8.** Simulated disease severity $\mathcal{V}$ of WSR (left) and WLR (right) across four locations: Bettendorf (A), Bicherhaff (B), Koerich (C), and Weiswampach (D), shown as a cross-section along the $x_1$-axis between May and July 2019.

with a MAPE of 15% and an RMSE of 0.91 percentage points. For WLR, the highest error was observed at Bettendorf, with a MAPE of 60% and an RMSE of 0.92 percentage points.

Fig. 10 presents the results of the two-dimensional spatial distribution of simulated severity of WSR and WLR in Bettendorf on May 24, June 5, and July 3, 2019. There is a clear increase in disease

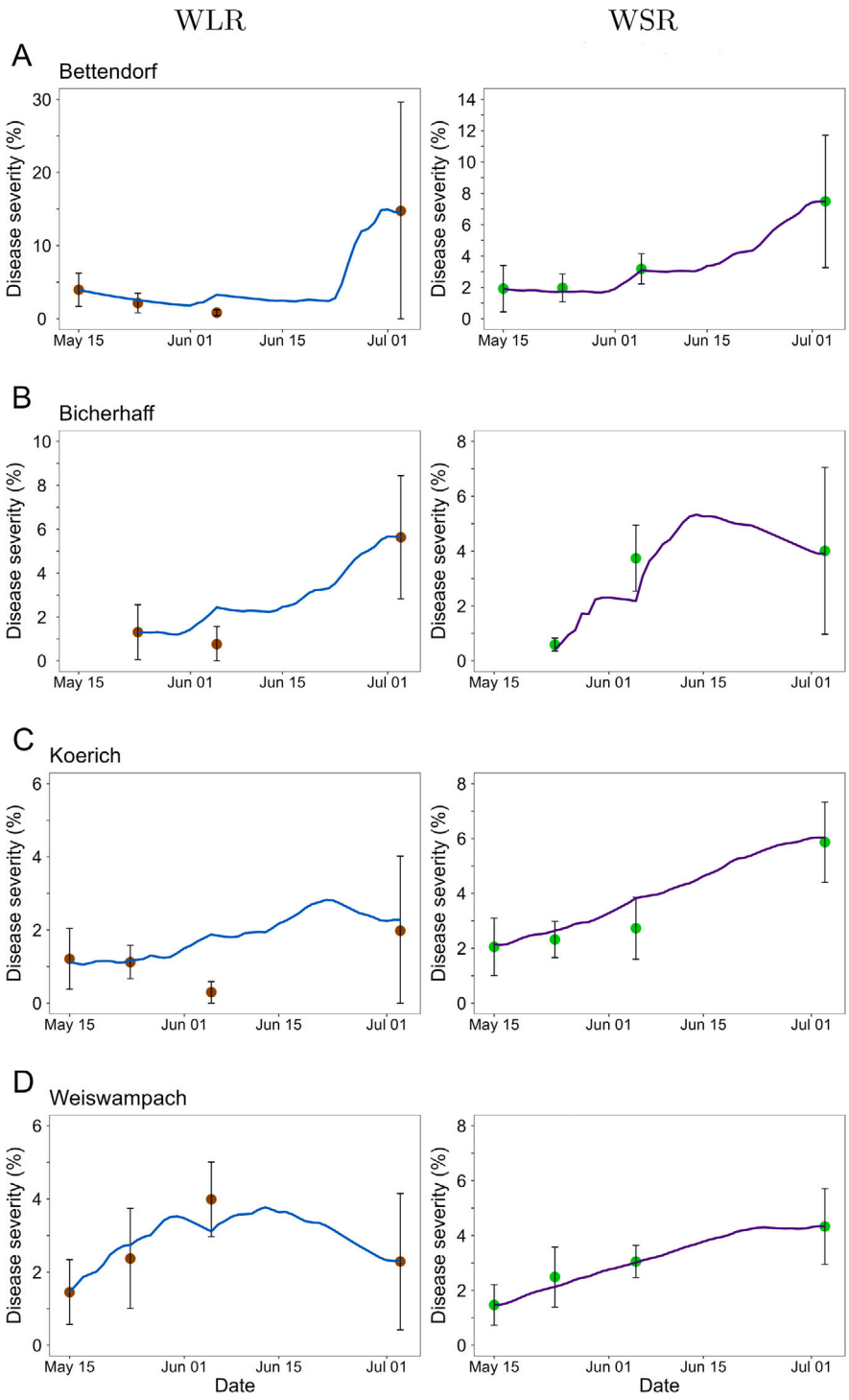


**Fig. 9.** Comparison between UAV imagery derived (circle) and SEIR-estimated (solid line) disease severity for WLR (right) and WSR (left) at Bettendorf (A), Bicherhaff (B), Koerich (C), and Weiswampach (D).

severity over time, with infected areas expanding from late May to early July. This temporal progression of disease severity reflects favorable environmental conditions to disease development. Results showed an elliptical spread pattern from the initial infection point, and the severity gradients, indicating active radial expansion.

When comparing WSR and WLR, the simulation results show that WLR has generally higher severity levels by July, indicating more rapid disease progression. These spatial and temporal patterns highlight the importance of early detection and targeted management to control the disease outbreaks.

## 4. Discussion

Wheat rust epidemics, particularly WSR and WLR arise from a complex interplay of host-pathogen interactions, environmental conditions, and management strategies. In this study, we present a non-autonomous spatiotemporal Susceptible-Exposed-Infected-Removed (SEIR) model to capture the dynamics of WSR and WLR across multiple representative sites of wheat-growing regions in Luxembourg. The model incorporates time- and weather-dependent variability in disease infectivity and severity, enabling a realistic representation of epidemic

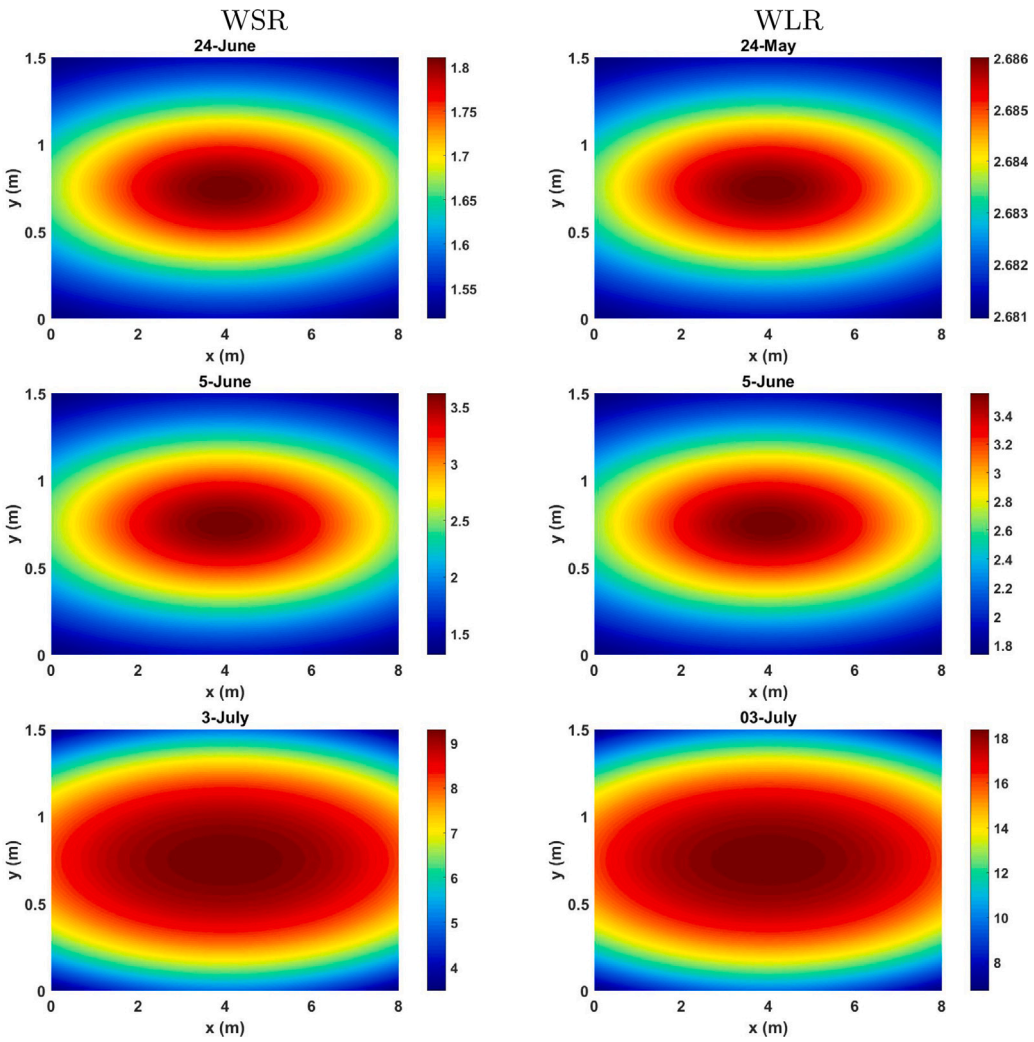


**Fig. 10.** Simulated 2D spatial distribution of disease severity $\mathcal{V}$ of WSR (left) and WLR (right) at three time points: 24-May, 5-June, and 3-July.

**Table 3**
Statistical indicators of the SEIR model's fit quality in simulating WSR and WLR severities.

| Disease | Site | MAE [prct point] | RMSE [prct point] | MAPE [%] |
|---|---|---|---|---|
| WSR | Bettendorf | 0.27 | 0.4 | 10 |
| | Bicherhaff | 0.56 | 0.91 | 15 |
| | Koerich | 0.42 | 0.16 | 5 |
| | Weiswampach | 0.09 | 0.14 | 3 |
| WLR | Bettendorf | 0.54 | 0.92 | 60 |
| | Bicherhaff | 0.37 | 0.64 | 49 |
| | Koerich | 0.34 | 0.58 | 81 |
| | Weiswampach | 0.34 | 0.55 | 10 |

MAE: mean absolute error; RMSE: root mean square error; MAPE: mean absolute percentage error.

development in fields. Changes in the number of host plants in each compartment followed coupled integro-differential equations where the influence of factors such as air temperature, relative air humidity, and wind on the progress of the diseases is considered. The modeling approach followed that of Segarra et al. (2001) and is an expansion of the mathematical model for spore dispersal described in El Jarroudi et al. (2020) with the integration of temperature-dependent latency periods and improved modeling of the different compartments.

Our SEIR models differ from the one proposed in Rimbaud et al. (2018) in both complexity and methodological approach. In their work, interactions between compartments are governed by probabilistic laws, and the dispersal mechanism is represented using a two-dimensional dispersal kernel that defines the probability of propagule spread. Propagules that land outside the simulated landscape are considered lost, as the model assumes an absorbing boundary condition with no external sources of propagules. In contrast, our models incorporate governing equations and coefficients that depend on both the disease life cycle and meteorological variables. Disease dynamics are assumed to follow the law of mass action, with transmission governed by a Neumann boundary condition imposing zero flux at the domain boundaries– ensuring no external influence on the system. The compartment structure can be extended to distinguish between susceptible resistant hosts and those that are exposed, infected, or removed, as well as to differentiate between the densities of virulent and avirulent pathogen strains over time (van den Bosch and Gilligan, 2003; Pietravalle et al., 2006; Lo Iacono et al., 2013). Beyond wheat rusts, the flexibility of the SEIR framework allows it to be adapted to other crop-pathogen systems. For instance, it could be tailored to study rust dynamics in barley, where differences in spore dispersal and weather conditions may substantially influence epidemic trajectories (Leonard and Szabo, 2005). Furthermore, integrating climate change projections into the model could provide valuable insights into how evolving weather patterns might affect the frequency and severity of such diseases.

Numerical simulations were carried out to visually assess the spatiotemporal patterns of the $S$, $E$, $I$ and $R$ densities over the computational domain $[0, 8] \times [0, 1.5]$ during the period of May to July 2019,

which corresponds to the critical period of WSR and WLR development at the study sites. The ability of the SEIR model to simulate spatially explicit disease dynamics supports targeted and efficient management strategies. For WSR, the localized nature of severity suggests that site-specific interventions, such as fungicide spot applications, may optimize resource use while minimizing environmental impact. In contrast, the spatial spread of WLR necessitates broader control measures, such as field-wide fungicide applications or the deployment of resistant cultivars. Apart from using agrochemicals to control wheat leaf and stripe rusts, other strategies to avoid the diseases or minimize their impacts include growing resistant wheat varieties and reducing the disease carryover from one cropping season to the next (overwintering survival of fungi) through crop rotation or tillage or intercropping (Dubin and Rajaram, 1996; Verreet et al., 2000; Cao et al., 2015).

In this study, our objective was to assess how effectively the SEIR model can replicate the development and intensity of WSR and WLR epidemics. Overall, the results showed good fit of the SEIR model in simulating disease severity compared to UAV data for WSR and WLR, with the inclusion of temperature and humidity variations. Temperatures in the range of 15–25 °C, combined with relative humidity above 75%, were associated with increased disease severity. These thresholds highlight the critical role of climate in influencing disease infection rates, indicating the importance of accurately capturing these dynamics in epidemic models. Because of the lack of long-term UAV imagery derived disease severity data, no validation of the SEIR models was carried out. The availability of such data, along with long-term datasets spanning multiple seasons and diverse management practices, will facilitate further model validation, and contribute to improve the model performance.

The presence of other foliar diseases, such as Septoria tritici blotch and powdery mildew, during the study period may have influenced the progression and severity of WSR and WLR, as their pathogens also depend on living plant tissue to complete their life cycles (Eversmeyer et al., 1988; Eversmeyer and Kramer, 2000). This could have affected the performance of the SEIR models (Table 3), which were designed to simulate only the development of WSR and WLR, without accounting for potential interactions with other diseases. Future research could explore the integration of other major foliar diseases (e.g., through the use of combined disease risk models) to more accurately capture the dynamics of rust diseases in wheat fields. Alternatively, the scope of the SEIR model can be expanded to include interactions with major foliar diseases, which would provide a more holistic understanding of disease dynamics.

The numerical simulations relied on several assumptions for model parameterization, with parameter values sourced from the literature (Table 2). For example, initial spore loads in the field, along with wind velocity and direction, were not empirically measured; this may have influenced the accuracy of simulated spore dispersal densities. Similarly, the UAV-based RGB imagery did not allow for differentiation between healthy plants, plants in latent stage and those that were infectious. Utilizing real-time wind direction and velocity data, as well as advanced remote sensing technologies, could improve the representation of pathogen dispersal. For instance, UAVs equipped with hyperspectral sensors have shown strong potential for monitoring spore dispersal patterns in other cropping systems (e.g., Hatala et al., 2010; Qin et al., 2023). Additionally, adopting a Bayesian modeling framework (e.g., Gibson et al., 2004), which enables the representation of uncertainty in unobserved system components, could help address some of the limitation inherent in our current modeling approach.

From an applied perspective, a key challenge in using SEIR model presented in this study within decision support tools to manage WSR and WLR epidemics lies in the potential interruption of disease progression by unfavorable environmental conditions such as sudden weather changes or concurrent foliar diseases. As a result, the disease may fail to reach the final severity levels predicted by the model, potentially leading to unnecessary control interventions if severe outbreaks are overestimated. To support risk-based decisions informed by weather forecasts, a promising approach is the use of multi-center or multi-model forecast ensembles, which can generate a range of possible outcomes and assess the likelihood of disease severity under varying future weather scenarios.

In summary, this study evaluated the effectiveness of SEIR model in simulating the progression and severity of WSR and WLR across different wheat growing regions in Luxembourg. A theoretical framework was proposed, and numerical simulations were conducted using disease severity estimates derived from UAV imagery. Overall, the SEIR model produced good simulations of the disease severity for both WSR and WLR, indicating reasonable fit quality. While the SEIR modeling approach showed promising potential, it also highlighted critical areas that require refinement and further investigation. To enhance robustness and applicability, future research should prioritize their validation across diverse agroecosystems and cropping systems. The modeling framework can be further extended to incorporate pathogen adaptation dynamics and host resistance mechanisms, and enriched with climate risk components, thereby enabling the development of adaptive, evidence-based disease management strategies under conditions of environmental uncertainty.

## CRediT authorship contribution statement

**Mustapha El Jarroudi:** Writing – original draft, Supervision, Methodology, Conceptualization. **Hasan Karjoun:** Writing – original draft, Software, Formal analysis, Visualization, Conceptualization. **Riane Hajjami:** Writing – original draft, Formal analysis, Conceptualization. **Louis Kouadio:** Writing –original draft, Methodology, Data curation, Visualization, Conceptualization. **Moussa El Jarroudi:** Writing – review & editing, Methodology, Investigation, Conceptualization.

## Declaration of competing interest

The authors declare that they have no known competing financial interests or personal relationships that could have appeared to influence the work reported in this paper.

## Acknowledgments

Disease data were from the project SENTINELLE, which was funded by the Ministry of Higher Education and Research of the Grand Duchy of Luxembourg and the Administration des Services Techniques de l'Agriculture. We are also grateful to Dr. Juergen Junk from the Luxembourg Institute of Science and Technology for providing the meteorological data. We thank Ramin Heidarian Dekhordi for providing UAV data.

## Data availability

The data that has been used is confidential.

## References

Andreu-Vaillo, F., Mazón, J., Rossi, J., Toledo-Melero, J., 2010. Nonlocal Diffusion Problems. vol. 165, American Mathematical Soc., p. 256. http://dx.doi.org/10.1090/surv/165.

Bates, P., Fife, P.C., Ren, V., Wang, X., 1997. Travelling waves in convolution model for phase transitions. Arch. Rat. Mech. Anal. 138, 105–136. http://dx.doi.org/10.1007/s002050050037.

van den Bosch, F., Frinking, H.D., Metz, J.A.J., Zadoks, J.C., 1988. Focus expansion in plant disease. III: Two experimental examples. Phytopathology 78, 919–925. http://dx.doi.org/10.1094/Phyto-78-919.

van den Bosch, F., Gilligan, C.A., 2003. Measures of durability of resistance. Phytopathology 93 (5), 616–625. http://dx.doi.org/10.1094/PHYTO.2003.93.5.616.

van den Bosch, F., Metz, J.A.J., Zadoks, J.C., 1999. Pandemics of focal plant disease, a model. Phytopathology 89, 495–505. http://dx.doi.org/10.1094/PHYTO.1999.89.6.495.

BSA, 2018. Beschreibende Sortenliste 2018. Getreide, mais, ölfrüchte, leguminosen (Großkörnig), Hackfrüchte (Außer Kartoffeln). Deutscher Landwirtschaftsverlag GmbH, Hannover, Germany.

Burie, J.-B., Calonnec, A., Langlais, M., 2008. Modeling of the invasion of a fungal disease over a vineyard. In: Deutsch, A., Parra, R.B.d.l., Boer, R.J.d., Diekmann, O., Jagers, P., Kisdi, E., Kretzschmar, M., Lansky, P., Metz, H. (Eds.), Mathematical Modeling of Biological Systems, Volume II: Epidemiology, Evolution and Ecology,Immunology, Neural Systems and the Brain, and Innovative Mathematical Methods. Birkhäuser Boston, Boston, MA, USA, pp. 11–21. http://dx.doi.org/10.1007/978-0-8176-4556-4_2.

Cao, S., Luo, H., Jin, M., Jin, S., Duan, X., Zhou, Y., Chen, W., Liu, T., Jia, Q., Zhang, B., Huang, J., Wang, X., Shang, X., Sun, Z., 2015. Intercropping influenced the occurrence of stripe rust and powdery mildew in wheat. Crop. Prot. 70, 40–46. http://dx.doi.org/10.1016/j.cropro.2014.12.008.

Cooke, B.M., Gareth, J.D., Kaye, B., 2006. The Epidemiology of Plant Diseases, second ed. Springer, Dordrecht, Netherlands, http://dx.doi.org/10.1007/1-4020-4581-6.

Cunniffe, N.J., Koskella, B., E. Metcalf, C.J., Parnell, S., Gottwald, T.R., Gilligan, C.A., 2015. Thirteen challenges in modelling plant diseases. Epidemics 10, 6–10. http://dx.doi.org/10.1016/j.epidem.2014.06.002.

Cunniffe, N.J., Stutt, R.O.J.H., van den Bosch, F., Gilligan, C.A., 2012. Time-dependent infectivity and flexible latent and infectious periods in compartmental models of plant disease. Phytopathology 102 (4), 365–380. http://dx.doi.org/10.1094/PHYTO-12-10-0338.

de Vallavieille-Pope, C., Huber, L., Leconte, M., Bethenod, O., 2002. Preinoculation effects of light quantity on infection efficiency of *Puccinia striiformis* and *P. Triticina* on wheat seedlings. Phytopathology 92 (12), 1308–1314. http://dx.doi.org/10.1094/PHYTO.2002.92.12.1308.

de Vallavieille-Pope, C., Huber, L., Leconte, M., Goyeau, H., 1995. Comparative effects of temperature and interrupted wet periods on germination, penetration, and infection of *Puccinia recondita* f. sp. *tritici* and *P. striiformis* on wheat seedlings. Phytopathology 85, 409–415. http://dx.doi.org/10.1094/Phyto-85-409.

Diekmann, O., Heesterbeek, J.A.P., 2000. Mathematical epidemiology of infectious diseases: model building, analysis and interpretation, vol. 5, John Wiley & Sons.

Diekmann, O., Othmer, H.G., Planqué, R., Bootsma, M.C.J., 2021. The discrete-timeKermack–McKendrick model: A versatile and computationally attractive framework for modeling epidemics. Proc. Natl. Acad. Sci. USA 118 (39), e2106332118. http://dx.doi.org/10.1073/pnas.2106332118.

Dubin, H., Rajaram, S., 1996. Breeding disease-resistant wheats for tropical highlands and lowlands. Annu. Rev. Phytopathol. 34 (1), 503–526. http://dx.doi.org/10.1146/annurev.phyto.34.1.503.

El Jarroudi, M., Karjoun, H., Kouadio, L., El Jarroudi, M., 2020. Mathematical modelling of non-local spore dispersion of wind-borne pathogens causing fungal diseases. Appl. Math. Comput. 376, 125107. http://dx.doi.org/10.1016/j.amc.2020.125107.

El Jarroudi, M., Kouadio, L., Bock, C.H., El Jarroudi, M., Junk, J., Pasquali, M., Maraite, H., Delfosse, P., 2017. A threshold-based weather model for predicting stripe rust infection in winter wheat. Plant Dis. 101, 693–703. http://dx.doi.org/10.1094/PDIS-12-16-1766-RE.

El Jarroudi, M., Kouadio, L., Delfosse, P., Tychon, B., 2014. Brown rust disease control in winter wheat: I. Exploring an approach for disease progression based on night weather conditions. Env. Sci. Pollut. Res. 21 (7), 4797–4808. http://dx.doi.org/10.1007/s11356-013-2463-6.

Eversmeyer, M.G., Kramer, C.L., 2000. Epidemiology of wheat leaf and stem rust in the central Great Plains of the USA. Annu. Rev. Phytopathol. 38 (1), 491–513. http://dx.doi.org/10.1146/annurev.phyto.38.1.491.

Eversmeyer, M.G., Kramer, C.L., Hassan, Z.M., 1988. Environmental influences on the establishment of *Puccinia recondita* infection structures. Plant Dis. 72, 409–412. http://dx.doi.org/10.1094/PD-72-0409.

FAO, 2019. New standards to curb the global spread of plant pests and diseases. The food and agriculture organization of the united nations (FAO). Rome, Italy. https://www.fao.org/news/story/en/item/1187738/icode/. (Accessed 16 January 2023).

Frantzen, J., van den Bosch, F., 2000. Spread of organisms: Can travelling and dispersive waves be distinguished? Basic Appl. Ecol. 1 (1), 83–92. http://dx.doi.org/10.1078/1439-1791-00010.

Gibson, G.J., Kleczkowski, A., Gilligan, C.A., 2004. Bayesian analysis of botanical epidemics using stochastic compartmental models. Proc. Natl. Acad. Sci. USA 101 (33), 12120–12124. http://dx.doi.org/10.1073/pnas.0400829101.

Gilligan, C.A., 2008. Sustainable agriculture and plant diseases: An epidemiological perspective. Philos. Trans. R Soc. Lond. B Biol. Sci. 363 (1492), 741–759. http://dx.doi.org/10.1098/rstb.2007.2181.

Gilligan, C.A., van den Bosch, F., 2008. Epidemiological models for invasion and persistence of pathogens. Annu. Rev. Phytopathol. 46 (1), 385–418. http://dx.doi.org/10.1146/annurev.phyto.45.062806.094357.

Gilligan, C.A., Gubbins, S., Simons, S.A., 1997. Analysis and fitting of an *SIR* model with host response to infection load for a plant disease. Philos. Trans. R Soc. Lond. B Biol. Sci. 352 (1351), 353–364. http://dx.doi.org/10.1098/rstb.1997.0026.

Gourley, S.A., Wu, J., 2006. Delayed nonlocal diffusion systems in biological invasion and diseases spread. In: Brunner, H., Zhao, X.-Q., Zou, X. (Eds.), Nonlinear Dynamics and Evolution Equations. vol. Fields Inst. Commun. 48, American Mathematical Society, Providence, RI, USA, pp. 137–200. http://dx.doi.org/10.1090/fic/048.

Hatala, J.A., Crabtree, R.L., Halligan, K.Q., Moorcroft, P.R., 2010. Landscape-scale patterns of forest pest and pathogen damage in the greater yellowstone ecosystem. Remote Sens. Environ. 114 (2), 375–384. http://dx.doi.org/10.1016/j.rse.2009.09.008.

Hau, B., de Vallavieille-Pope, C., 2006. Wind-dispersed diseases. In: Cooke, B., Jones, D.G., Kaye, B. (Eds.), The Epidemiology of Plant Diseases. Springer, Dordrecht, Netherlands, pp. 387–416. http://dx.doi.org/10.1007/1-4020-4581-6_15.

Heidarian Dehkordi, R., Denis, A., Fouche, J., Burgeon, V., Cornelis, J.T., Tychon, B., Placencia Gomez, E., Meersmans, J., 2020b. Remotely-sensed assessment of the impact of century-old biochar on chicory crop growth using high-resolution UAV-based imagery. Int. J. Appl. Earth Obs. Geoinf. 91, 102147. http://dx.doi.org/10.1016/j.jag.2020.102147.

Heidarian Dehkordi, R., El Jarroudi, M., Kouadio, L., Meersmans, J., Beyer, M., 2020a. Monitoring wheat leaf rust and stripe rust in winter wheat using high-resolution UAV-based red-green-blue imagery. Remote. Sens. 12 (22), 3696. http://dx.doi.org/10.3390/rs12223696.

Jane White, K., Gilligan, C., 2006. The role of initial inoculum on epidemic dynamics. J. Theoret. Biol. 242 (3), 670–682. http://dx.doi.org/10.1016/j.jtbi.2006.04.004.

Kirtphaiboon, S., Humphries, U., Khan, A., Yusuf, A., 2021. Model of rice blast disease under tropical climate conditions. Chaos Solitons Fractals 143, 110530. http://dx.doi.org/10.1016/j.chaos.2020.110530.

Legg, B., 1983. Movement of plant pathogens in the crop canopy. Philos. Trans. R. Soc. Lond. B, Biological Sci. 302 (1111), 559–574.

Leonard, K.J., Szabo, L.J., 2005. Stem rust of small grains and grasses caused by *Puccinia graminis*. Mol. Plant Pathol. 6 (2), 99–111. http://dx.doi.org/10.1111/j.1364-3703.2005.00273.x.

Lo Iacono, G., van den Bosch, F., Gilligan, C.A., 2013. Durable resistance to crop pathogens: an epidemiological framework to predict risk under uncertainty. PLOS Comput. Biol. 9 (1), e1002870. http://dx.doi.org/10.1371/journal.pcbi.1002870.

Madden, L., 1997. Effects of rain on splash dispersal of fungal pathogens. Can. J. Plant Pathol. 19 (2), 225–230. http://dx.doi.org/10.1080/07060669709500557.

Madden, C.V., Hughes, G., van den Bosch, F., 2007. The Study of the Plant Disease Epidemics. The American Phytopathological Society, St. Paul, MN, USA.

Mikaberidze, A., Mundt, C.C., Bonhoeffer, S., 2016. Invasiveness of plant pathogens depends on the spatial scale of host distribution. Ecol. Appl. 26 (4), 1238–1248. http://dx.doi.org/10.1890/15-0807.

Narouei-Khandan, H.A., Shakya, S.K., Garrett, K.A., Goss, E.M., Dufault, N.S., Andrade-Piedra, J.L., Asseng, S., Wallach, D., Bruggen, A.H.v., 2020. BLIGHTSIM: A new potato late blight model simulating the response of *Phytophthora infestans* to diurnal temperature and humidity fluctuations in relation to climate change. Pathogens 9 (8), 659. http://dx.doi.org/10.3390/pathogens9080659.

Othmer, H.G., Dunbar, S.R., Alt, W., 1988. Models of dispersal in biological systems. J. Math. Biol. 26 (3), 263–298. http://dx.doi.org/10.1007/BF00277392.

Pan, S., Li, W.-T., Lin, G., 2009. Travelling wave fronts in nonlocal delayed reaction-diffusion systems and applications. Z. Für Angew. Math. Und Phys. 60 (3), 377–392. http://dx.doi.org/10.1007/s00033-007-7005-y.

Papastamati, K., van den Bosch, F., 2007. The sensitivity of the epidemic growth rate to weather variables, with an application to yellow rust on wheat. Phytopathology 97 (2), 202–210. http://dx.doi.org/10.1094/PHYTO-97-2-0202.

Pietravalle, S., Lemarié, S., van den Bosch, F., 2006. Durability of resistance and cost of virulence. Eur. J. Plant Pathol. 114, 107–116. http://dx.doi.org/10.1007/s10658-005-3479-7.

Qin, W., Chen, P., He, R., 2023. Study on the dynamic distribution of spores of powdery mildew pathogen in wheat by rotor airflow of plant protection UAV. PLoS One 18 (11), 1–13. http://dx.doi.org/10.1371/journal.pone.0288248.

Rimbaud, L., Papaïx, J., Rey, J.-F., Barrett, L.G., Thrall, P.H., 2018. Assessing the durability and efficiency of landscape-based strategies to deploy plant resistance to pathogens. PLoS Comput. Biol. 14 (4), e1006067. http://dx.doi.org/10.1371/journal.pcbi.1006067.

Sackett, K.E., Mundt, C.C., 2005. Primary disease gradients of wheat stripe rust in large field plots. Phytopathology 95 (9), 983–991. http://dx.doi.org/10.1094/PHYTO-95-0983.

Savary, S., Nelson, A., Willocquet, L., Pangga, I., Aunario, J., 2012. Modeling and mapping potential epidemics of rice diseases globally. Crop. Prot. 34, 6–17. http://dx.doi.org/10.1016/j.cropro.2011.11.009.

Segarra, J., Jeger, M.J., van den Bosch, F., 2001. Epidemic dynamics and patterns of plant diseases. Phytopathology 91, 1001–1010. http://dx.doi.org/10.1094/PHYTO.2001.91.10.1001.

Sinha, P., Chen, X., 2021. Potential infection risks of the wheat stripe rust and stem rust pathogens on barberry in Asia and southeastern Europe. Plants 10 (5), 957. http://dx.doi.org/10.3390/plants10050957.

Soubeyrand, S., Held, L., Höhle, M., Sache, I., 2008. Modelling the spread in space and time of an airborne plant disease. J. R. Stat. Soc. Ser. C. Appl. Stat. 57 (3), 253–272. http://dx.doi.org/10.1111/j.1467-9876.2007.00612.x.

Tabonglek, S., Humphries, U.W., Khan, A., 2022. Mathematical model for rice blast disease caused by spore dispersion affected from climate factors. Symmetry 14 (6), 1131. http://dx.doi.org/10.3390/sym14061131.

Verreet, J.A., Klink, H., Hoffmann, G.M., 2000. Regional monitoring for disease prediction and optimization of plant protection measures: The IPM wheat model. Plant Dis. 84 (8), 816–826. http://dx.doi.org/10.1094/PDIS.2000.84.8.816.

Xiao, Y., Dong, Y., Huang, W., Liu, L., 2022. Regional prediction of fusarium head blight occurrence in wheat with remote sensing based susceptible-exposed-infectious-removed model. Int. J. Appl. Earth Obs. Geoinf. 114, 103043. http://dx.doi.org/10.1016/j.jag.2022.103043.

Zadoks, J.C., 1971. Systems analysis and the dynamics of epidemics. Phytopathology 61, 600–610. http://dx.doi.org/10.1094/Phyto-61-600.